NUREG/CR-2777

ANL-80-108

NUREG/CR-2777

ANL-80-108

THE RELEASE OF FISSION GAS DURING TRANSIENT HEATING OF LWR FUEL

by

Stephen M. Gehl

ARGONNE NATIONAL LABORATORY

ARGONNE NATIONAL LABORATORY, ARGONNE, ILLINOIS

Prepared for the Office of Nuclear Regulatory Research
U. S. NUCLEAR REGULATORY COMMISSION
under Interagency Agreement DOE 40-550-75

Available from

GPO Sales Program
Division of Technical Information and Document Control
U. S. Nuclear Regulatory Commission
Washington, D.C. 20555

and

National Technical Information Service
Springfield, Virginia 22161

NUREG/CR-2777
ANL-80-108
(Distribution
Code: R3)

ARGONNE NATIONAL LABORATORY
9700 South Cass Avenue
Argonne, Illinois 60439

THE RELEASE OF FISSION GAS DURING TRANSIENT HEATING OF LWR FUEL

by

Stephen M. Gehl

Materials Science Division

Manuscript Completed
March 1981

Published
May 1982

Prepared for the Division of Reactor Safety Research
Office of Nuclear Regulatory Research
U. S. Nuclear Regulatory Commission
Washington, D. C. 20555
Under Interagency Agreement DOE 40-550-75

NRC FIN No. A2016

THE RELEASE OF FISSION GAS DURING TRANSIENT HEATING OF LWR FUEL

by

S. M. Gehl

ABSTRACT

The direct electrical heating technique was used to study fission-gas release and mechanical behavior of irradiated light-water reactor (LWR) fuels during thermal transients. An empirical correlation between fission-gas release and transient temperature history was developed for power-cooling mismatch (PCM) and anticipated transients. Gas release during the refill portion of a design-basis loss of cooling accident was estimated to be less than 1%. Fission-gas release during PCM accidents was found to be controlled by intergranular microcracking and the interlinkage of tunnels on grain edges. For high-gas-release transients, the fractional gas release was shown to be equal to the fractional coverage of grain boundaries by microcracks. Temperature calculations indicated that microcracking causes a significant decrease in the fuel thermal conductivity.

NRC FIN No.	FIN Title
A2016	Transient Fuel Response and Fission-Product Release

TABLE OF CONTENTS

TABLE OF CONTENTS

LIST OF FIGURES

LIST OF FIGURES

LIST OF FIGURES

LIST OF TABLES

THE RELEASE OF FISSION GAS DURING TRANSIENT HEATING OF LWR FUEL[a]

by

S. M. Gehl

EXECUTIVE SUMMARY

The large amounts of gaseous fission products produced during the irradiation of light water reactor fuels have several important effects on the performance and safe operation of reactors during normal and upset conditions. Fission gas released from the UO_2 fuel pellets can reduce the thermal conductivity of the fuel-rod fill gas and thus increase fuel temperature for a given rod power. The higher temperature increases the stored energy of the rod and can cause additional release of fission products. An initial release of fission gas can also affect the subsequent release of other fission products by altering the fuel microstructure. Finally, the radioactive isotopes of the gaseous fission products make an important contribution to the radiological source term during reactor accidents.

The release of fission gas during all stages of reactor operation up to design-basis accidents is addressed during the licensing of a nuclear reactor. For design-basis events, i.e., loss-of-cooling and control-rod-ejection accidents, the U. S. Nuclear Regulatory Commission has set forth values of fission-product release to be used in estimating the radiological consequences of the accidents. These licensing assumptions are intended to be conservative estimates of the actual fission-product release. For normal operating conditions and for upset conditions less severe than the design bases, licensing analyses are usually performed by applying a fuel-rod performance code that incorporates a model for estimating gas release. The models are usually based on the physics of the fission-gas release processes (often in a simplified form) and are generally calibrated against available data on fission-gas release.

However, the analytical predictions of gas release often exhibit wide variances with the data they are intended to reproduce. This situation is due to (1) an incomplete knowledge of the relevant physical processes responsible for the release of fission gas; and (2) errors and uncertainties in the calculation of the fuel temperature, which strongly influences gas release.

This report describes the results of a study undertaken to improve the accuracy of predictions of fission-gas release by improving the understanding of the processes responsible for fission-gas transport and release from fuel. The study consisted of experimental determinations of fission-gas behavior under a variety of transient heating conditions. The experiments

---

[a]RSR FIN Budget No. A2016; RSR Contact: G. P. Marino

were performed out of reactor on irradiated fuels by use of the direct electrical heating technique. The experimental results were used to develop empirical correlations between fission-gas release and transient thermal history. The results also provided quantitative information on the physical mechanisms of gas transport and release. The mechanistic picture and data base obtained in the program were used in the development of a physically realistic computer code, GRASS-SST, for the prediction of fission-gas behavior. Only the experimental portion of the program is described in this report. The code-development activities are covered in a separate series of reports.

In the experiments, fission-gas release was measured as a function of maximum transient fuel temperature and transient heating rate. Maximum fuel temperature was varied from 1500 K to greater than the UO_2 melting point, while heating rate was varied from 5 to 300 K/s. These conditions are in the range of power-cooling mismatch events, although two experiments simulating loss-of-coolant conditions were performed. The high heating rates characteristic of rod-ejection accidents could not be achieved in the test equipment. A further variable addressed in the test series was the effect on fission-gas release of mechanically constraining the fuel column, as would occur if the Zircaloy cladding had collapsed onto the fuel pellets.

These experiments showed that fission-gas release was sensitive to both maximum temperature and heating rate. The following empirical correlation was developed to describe the gas release data:

$$Z = k_2 \, T_{cm}^{5.70} \, (dT/dt)^{-0.346} ,$$

where Z is the gas release expressed as a percent, T_{cm} is the maximum fuel centerline temperature in K, (dT/dt) is the heating rate at the fuel centerline in K/s, and k_2 is a constant equal to 7.58×10^{-19} for unconstrained fuel and 2.02×10^{-19} for constrained fuel. Thus, the application of mechanical constraint was found to reduce fission-gas release by a factor of 3.76 for equivalent transient temperature histories.

Two transient-induced microstructural processes were found to control fission-gas release during the experiments. In the first of these, fission-gas bubbles that collect along the grain boundaries and edges form tunnels that become interlinked over long distances through the fuel and thus vent gas to the external surfaces. In the second process, intergranular microcracks propagate through the fuel structure. The microcracking process appears to be a function of the local stress and temperature and is enhanced by the presence of fission-gas bubbles on the grain boundaries. Long-range interlinkage of the microcracks occurs when the microcrack coverage of the grain surface exceeds 40% of the total area of grain boundaries. Above this value, fractional fission-gas release is equal to the fraction of the grain surface area covered by microcracks. The relative importance of the two modes of fission-gas release depends largely on the transient heating rate. At lower heating rates, the observed gas release is primarily the result of tunnel interlinkage; for heating rates greater than ~50 K/s, microcrack interlinkage is the dominant mode of gas release.

The occurrence of microcracking during transient heating decreases the effective fuel thermal conductivity in proportion to the amount of microcracking. Locally, the thermal conductivity can be reduced to less than half of the value of uncracked fuel. The lower thermal conductivity can lead to significantly higher fuel temperatures both during a transient and in subsequent reactor operation.

With respect to particular accident sequences, the experimental results lead to the following conclusions:

During the initial stages of a control-rod ejection accident, microcracking is expected to cause the release of a significant portion of the grain-boundary gas prior to fuel melting. (Note that this conclusion is based on an extrapolation of the test data, since the high heating rates of the rod-ejection accident were not attained in the experiments.) A reevaluation of the current licensing assumption is recommended to account for the potential early release. An assumption of 30% release prior to melting, rather than the 10% now used, appears to be more realistic. This change is expected to have a relatively small effect on assessments of overall reactor safety.

The results of the power-cooling mismatch simulations are directly applicable to the study of fission-gas release during American National Standards Institute Condition II events. Gas release during such transients is low, and the resulting effect on gap conductance is minimal. However, the potential for microcracking should be considered in calculating fuel temperatures during and after the transient.

The studies of loss-of-coolant conditions indicate that fission-gas release during the refill portion of a design-basis loss-of-coolant accident will be 1% or less. The empirical correlation described above gives a conservative estimate of fission-gas release for these conditions. For accidents that go beyond the design basis, microcracking, thermal shock, fuel chemical reactions, and fuel melting may cause the release of nearly all of the fission gas from the fuel.

Finally, the direct electrical heating technique has been shown to be a useful tool for the simulation of fuel response to reactor accidents under well-controlled thermal conditions. Many of the phenomena associated with severe fuel damage events, e.g., fission-product release, Zircaloy oxidation, clad ballooning and rupture, fuel-Zircaloy reactions, and thermal shock, can be studied in appropriately designed out-of-reactor test equipment.

I. INTRODUCTION AND LITERATURE REVIEW

Large amounts of gaseous fission products are produced during the irradiation of light water reactor (LWR) fuels. The fission products that are usually considered "gaseous" are the noble gases krypton and xenon, and the halogen iodine.[1] Although elemental iodine is not thermodynamically stable under the conditions of an operating fuel rod, the transport properties of iodine often resemble those of a gas. The cumulative yield of krypton, xenon, and iodine exceeds 125 atoms per 100 fissions.[1]

Fission gases have several important effects on the performance and safe operation of nuclear reactors during both normal and upset conditions. First, fission gases that escape from a UO_2 pellet decrease the thermal conductance of the fuel-cladding gap, and thus alter the relationship between reactor power and fuel temperature. Knowledge of the changing concentration of fission products in the fill gas is therefore needed for the prediction of temperatures over the life of a fuel rod. Second, the release of fission gases will, under some circumstances, create a stable network of interconected tunnels that aid the subsequent release of other fission products. The secondary release of fission products may include species such as iodine, cadmium, and tellurium, which can chemically attack the Zircaloy cladding and contribute to stress-corrosion cracking. Third, since the gaseous fission proudcts are highly mobile, their radioactive isotopes make an important contribution to the radiological source term during reactor accidents. This circumstance occurred during the accident at the Three Mile Island-2 (TMI-2) reactor, in which large amounts of krypton, xenon, and iodine were released into the reactor containment building.[2]

The release of fission products during design-basis accidents is addressed during the licensing of a nuclear reactor. In the Regulatory Guides, the U. S. Nuclear Regulatory Commission (NRC) sets forth values of fission-product release to be used in determining the radiological consequences of loss-of-cooling accidents (LOCAs) and control-rod ejection accidents. These licensing assumptions are intended to be conservative estimates of the actual fission-product release. For a LOCA, the licensing assumption is that 25% of the iodine and 100% of the noble gases are available for release from the reactor containment.[3,4] In a rod-ejection accident, 10% of the iodine and noble gases are assumed to be released from fuel that does not melt, while 25% of the iodine and 100% of the noble gases are assumed to be released from fuel that exceeds the melting point.[5] One of the goals of the present study is an assessment of the conservatism of these assumptions.

The study of fission-gas transport and release phenomena requires accurate knowledge of parameters such as fuel-rod plenum pressure, local fuel temperatures, and temperature gradients. In the case of transient heating, the rate of change of these parameters is also important. Although fission-gas release from commercial power reactors is often measured, fuel temperatures and plenum pressures are seldom measured. However, instrumentation for the collection of this information can be installed with some difficulty in test reactors, and more easily in out-of-reactor test equipment. As a result, studies of fission-gas transport and release are usually performed by simulating power-reactor conditions in test reactors or in out-of-reactor experiments.

The open literature contains reports of a number of in-reactor and out-of-reactor experiments designed to study fission-gas-release phenomena.[6-13] The utility of such experiments is sometimes difficult to evaluate because of the large variations in the accuracy with which the gas-release, temperature, and pressure data are measured, as well as in the faithfulness with which conditions expected in power reactors are duplicated. As a general rule, the experiments performed in test reactors give better simulations of power-reactor conditions such as neutron flux and radial temperature profile, while the out-of-reactor experiments permit the gas-release fraction and thermal history to be determined with greater absolute accuracy. All simulation experiments depart to some extent from power-reactor conditions. The differences and their effect on fission-gas release and fuel behavior must be evaluated to determine the applicability of simulation techniques to the study of gas-release phenomena in power reactors.

Most of the existing work on fission-gas effects concerns steady-state operation. The results of several such investigations have been used by the NRC in formulating the licensing assumptions.[3-5] In addition, the NRC is funding additional research aimed at determining the degree to which the licensing assumptions accurately reflect conditions typical of reactor accidents.

This report describes the results of one study, commissioned by the NRC, to investigate fission-gas transport and release phenomena. The study consisted of experimental determinations of fission-gas behavior under a variety of transient heating conditions. The experimental results were used to develop empirical correlations between fission-gas release and transient thermal history. The results also provided information on the physical mechanisms of gas transport and release. The mechanistic picture and data base obtained in the program were used in the development and verification of a physically realistic computer code, GRASS-SST, for the prediction of fission-gas behavior. This report is limited to the experimental portion of the program. Descriptions of the GRASS-SST code can be found elsewhere.[14-15] In the present program, thermal transients typical of two types of accident conditions were imposed on irradiated LWR fuel obtained from commercial and test reactors. The transient heating experiments were performed out of reactor using the direct electrical heating (DEH) technique.[16,17] The amount of fission gas released during the experiments was measured, and the accompanying microstructural changes were quantitatively characterized. Special emphasis was placed on the transient-induced microstructural changes, because they were found to be closely related to the physical processes of fission-gas release. The results of the DEH test program, including the posttest characterization, were used to develop a tentative picture of the mechanisms of fission-gas release. This picture was checked and refined by performing additional DEH tests. Models developed from the mechanisms were tested in the GRASS-SST code, thus providing additional confirmation of the validity of the mechanistic picture.

The current understanding of gas-release processes will be briefly reviewed to place the present results in perspective. Stable networks of intergranular porosity have long been observed in the columnar- and equiaxed-grain zones of oxide fuels, primarily in high-temperature liquid-metal fast-breeder reactor (LMFBR) irradiations. This porosity is generally "open", i.e., connected to the exterior surface. The presence of such porosity networks

reduces the effective diffusion distance required for gas release from approximately the pellet radius to approximately the grain radius. Thus, greatly enhanced fission-gas release is expected from fuels with stable, interconnected, intergranular porosity. This result has been confirmed by the observed low fission-gas content of equiaxed- and columnar-grain structures.[13,18] Note that the mechanisms by which equiaxed and columnar grains are formed, i.e. grain-boundary and lenticular-void motion, also contribute to the release of fission gas. However, a stable network of intergranular porosity can be generated without reforming the grain structure. Tubular porosity along the grain edges has been found to be stable when the associated swelling reaches a minimum value of 7%.[19-21] For swelling less than the critical value, the stable morphology consists of isolated bubbles along the grain edges. The critical swelling for edge-tunnel stability is used as an interconnection criterion in GRASS-SST.[14] Code predictions based on this model indicate that interconnection of the grain-edge porosity and a resulting burst release of fission gas can occur during steady-state operation to high burnups with no significant grain growth.[14]

In experimental irradiations of UO_2 at 2020 K reported by Tucker,[22,23] interlinkage of grain-edge tunnels was observed at burnups as low as 0.25%. Here, early interlinkage was promoted by high temperatures and the absence of mechanical constraint. The published fractographs show isolated bubbles on the grain surfaces as well as grain-edge tunnels. Killeen[24] has observed interconnected sinuous channels on grain surfaces in Cr_2O_3-doped UO_2 irradiated at 1780 K to a burnup of 0.3%. These results contrast with observations for power reactors, in which low temperatures delay interconnection until high burnup is reached.

Current understanding of the release of intergranular fission gas can be summarized by stating that interconnected intergranular porosity is known to vent fission gas, and that the conditions under which long-range interconnection occurs during steady-state irradiation are well understood. The present report focuses on the modes of interconnection that dominate during transient heating. The results of this program demonstrate that planar intergranular separations, in addition to grain-edge tunnels, make an important contribution to transient fission-gas release.

Two types of reactor accidents, the power-cooling mismatch (PCM) and the above-mentioned LOCA, were studied in this program. The term "power-cooling mismatch" refers to an imbalance between the rate of fission heating and the rate of heat removal. A PCM can be caused by a turbine trip, cold water injection, rapid control rod movements, or the like. A schematic fuel-temperature history for a typical PCM is shown in Fig. 1. The center temperature increases at $\sim$9 K/s, while the surface temperature remains nearly constant. As a result, the radial temperature gradient increases continually. Note that center temperature and radial temperature gradient are strongly coupled during the accident.

In a LOCA, a break in the primary coolant system leads to system depressurization and the escape of coolant through the break. If, as a result, the water in the core boils away, heat removal is seriously impaired. Under these conditions, fuel temperatures will rise at a rate determined by stored energy, fission-product decay heat, steam oxidation of Zircaloy, and the rate of heat transfer at the cladding-steam interface.

(Fission heating is ended owing to the loss of the moderator.) The LOCA can be terminated by the operation of the emergency core cooling system (ECCS); if not terminated, it can lead to fuel melting. A schematic temperature history for the blowdown and heatup portions of a LOCA is shown in Fig. 2. During heatup, there is little difference between the center and surface temperatures, in contrast to the PCM temperature history.

Because of the complexity of these two temperature histories, their duplication in an out-of-reactor environment is difficult. The approaches used for the simulation of PCM and LOCA thermal conditions are described in the next section.

II. EXPERIMENTAL PROCEDURE

A. The Direct Electrical Heating Technique

Direct electrical heating of UO_2 produces radial temperature profiles that are similar to those obtained by fission heating. As a result, DEH has been used for several studies of fuel and fission-product behavior.[6,7,10]

In DEH, electric current flows axially through a stack of fuel pellets. The ohmic heating of the fuel, coupled with cooling provided by flowing helium in the test chamber, produces a radial temperature profile that is close to the profile usually taken to represent "ideal" nuclear heating. As shown in Fig. 3, the temperature is highest at the fuel center, while the radial temperature gradient is zero at the fuel center and increases with increasing distance from the centerline. That is, the radial temperature profile is "convex down".

Nuclear heating and DEH differ in the radial distribution of energy deposition. Nuclear heating is characterized by a radial neutron flux depression, which keeps the energy deposition rate higher in the outer portion of the pellet than toward the center. The situation is reversed for electrical heating. Since the electrical conductivity of UO_2 increases with increasing temperature, the energy deposition rate during DEH is highest at the pellet centerline. As a result, the radial temperature profile produced by DEH decreases more rapidly with distance from the center than the nuclear heating profile (see Fig. 3).

Actually, both nuclear heating in power reactors and DEH depart from the ideal behavior described above. Cracks in the fuel, produced during start-up and shutdown, distort the temperature profile under nuclear heating conditions by several mechanisms: (1) Macrocracks distort the heat flow paths because of the difference in conductance. (2) Some of the fuel chunks formed by macrocracking can move into close thermal contact with the cladding, thus lowering their temperature relative to the remaining pieces. (3) Macrocracks can cause local inhomogeneities in the neutron flux, and therefore the heat generation rate. For electrical heating, macrocracks can distort the radial flux of heat and the axial flux of electricity. (A technique developed to alleviate the latter problem is described in Section II.A.2). During transient nuclear and electrical heating, high densities of microcracks can develop. These can decrease the effective thermal conductivity by a factor approaching 1/2, and thereby further distort the radial temperature profile.

These departures from ideal behavior are of the same order of magnitude as the departure caused by the inherent differences between nuclear and electrical heating. Therefore, it is not surprising that a study conducted as a part of this program showed no detectable difference between nuclear heating and DEH in the transient response of irradiated fuel as measured by the fission-gas behavior.[25] Because of its similarities to nuclear heating, combined with low cost, DEH is a powerful technique for studying fission-gas and fuel behavior during thermal transients.

1. DEH Test Apparatus

Two separate test chambers were used for the DEH experiments. The original design, shown schematically in Fig. 4, was used for the first three years of the program. An improved design, shown in Fig. 5, was used for the final year.

In both designs, a stack of pellets is held vertically between two tungsten electrodes. Each stack consists of a central pellet of irradiated fuel sandwiched between two pellets of unirradiated UO_2. The outer, or spacer, pellets accommodate axial temperature gradients between the stack and the tungsten electrodes and help keep temperatures uniform in the central test pellet.

The bottom electrode is fixed, but the upper electrode can move vertically. The upper electrode is attached to the chamber with a springy metal bellows and can slide within a cylindrical positioning guide. The system was designed so that the bellows tension exerts a light axial load on the specimen. A dead load of $\sim$2 N was also applied to the specimen to simulate the accumulated load on a typical pellet in a fuel rod. (A 2-N force corresponds to a stack of pellets $\sim$0.3 m high.)

A direct current of up to 125 A is supplied to the test specimen through the electrodes. The power supply and control circuitry are designed to accommodate the large change in specimen resistance that occurs as the UO_2 is heated.[17] During a transient, the power dissipated in the pellet stack is increased at a preprogrammed rate in order to produce the desired thermal history. Fuel-centerline heating rates in the range 2-500 K/s can be produced by this power supply.

A flowing stream of helium passes through the chamber to cool the test specimen and carry away the fission gas released from the fuel. The systems provide a controlled linear flow rate of up to 1 m/s at the specimen surface. After exiting the test chamber, the coolant passes through a series of particulate filters designed to remove condensable fission products from the stream. The fission gases carried along with the flowing helium stream are collected by passing the gas through an activated charcoal trap cooled by liquid nitrogen. After the test, the trapped gases are recovered by heating the charcoal. The total amount of gas collected, its chemical composition, and the krypton and xenon isotopic composition are then determined.

Up to this point, the description of the test equipment applies to both test chamber designs. The most important difference between the two chambers is the addition of a cylindrical tungsten mesh heater surrounding the specimen in the newer design. This external heater was used, in conjunction

with DEH, for the studies of LOCA-like conditions (see Section III.C). The external heater was also used for preheating the specimen prior to the initiation of DEH. Preheating is necessary to decrease the electrical resistance of the pellet to a level at which electric current will flow at a potential drop of a few hundred volts, and to volatilize the organic binder used in the specimen preparation procedure (see Section II.A.2). In the original DEH chamber, preheating was accomplished by shining a focused line heater on the specimen through the fused quartz chamber window. The major limitation of this technique was that the specimen was heated from one side only. As a result, "hot spots" sometimes developed as the direct electrical current followed the low-conductivity, i.e., hot, path down the side of the specimen. The cylindrical tungsten mesh heater incorporated in the replacement chamber produced a uniform heating pattern, and thus prevented hot spots during DEH.

2. Specimen Preparation Procedure

The thermal shock accompanying reactor start-up and shutdown produces a network of large cracks in oxide fuels. Because of the low irradiation temperatures experienced by the fuels used in the present program, crack healing did not occur. As a result, in their postirradiation state, the individual pellets were divided into 5-20 fragments held in place by the Zircaloy cladding. However, the cladding must be removed before DEH testing, because if left in place, it would provide a higher-conductivity path for the electric current and prevent heating of the fuel. Thus, an alternative means of retaining the cylindrical geometery of the fuel pellets and fixing the relative positions of the fragments was needed. In addition, early tests indicated that the displacement of pellet fragments during irradiation and handling frequently results in poor electrical contact between adjacent fragments. A specimen-preparation technique was therefore developed which produces usable DEH specimens from the fragmented Robinson fuel pellets through use of a UO_2 slip. The slip fills the free space between pellet fragments, thereby incorporating all the pieces into the electrical circuit and preventing relative motion of the fragments. Table I[26] gives the composition of the slip, which is a suspension of fine UO_2 powder ($\sim$0.6-μm particle diameter) in an aqueous solution of organic binders.

TABLE I. Composition of UO_2 Slip

0.6-μm depleted UO_2 powder, g	400	Distilled water, mL	300
Ammonium alginate,[a] g	2.0	Ammonium hydroxide, drops	15
Hydroxypropyl methylcellulose,[b] g	2.0		

[a]Kelco Superloid.

[b]Dow Methocel F4M.

Sections of clad fuel $\sim$150 mm in length are impregnated with slip using the apparatus shown in Fig. 6. One end of the fuel section is connected, by means of a compression fitting, to a lever-actuated grease gun;

a vacuum line is connected to the other end. The grease gun is used to pump slip into pellet interfaces and cracks, and into the gap between the fuel and cladding. The clad fuel is evacuated before the slip is injected to prevent the formation of trapped air pockets, which might expand and drive the slip out of the cracks when the injection pressure is released. The impregnated fuel lengths are allowed to dry for ∿2 days in air at room temperature and are then cut into a number of smaller pieces, each containing a single pellet.

The next step in the specimen-preparation procedure is the removal of the Zircaloy cladding section from the pellets. Since there is no metallurgical bonding of the cladding to the fuel in the Robinson fuel rods, the cladding can be slid off the fuel while flat-ended cylindrical rods hold the pellet ends fixed and parallel. Limited success has been achieved in producing free-standing pellets in this way. However, the pellets are fragile, making remote handling difficult. To remedy this situation, the test specimens were loaded into nonconductive cylindrical holders as the cladding was removed. Two holder designs were used, as shown in Fig. 7. A loose-fitting quartz tube was used for tests in which the pellets were radially unconstrained. For other tests, the fuel specimen was pushed into a close-fitting boron nitride sleeve, which was backed up by a stainless steel holder. This design provided the maximum readily achievable level of radial constraint.

To load either type of specimen holder, a tungsten disk (for the lower electrode) is placed in the holder followed by an unirradiated UO_2 pellet. The holder and clad, irradiated fuel pellet are then placed in a device that holds the fuel pellet fixed while the cladding is slid off and the holder is slid into place. A second unirradiated pellet is placed in the holder on top of the fuel pellet. The completed specimens are placed between the electrodes in the specimen chamber. Electrical contact with the lower electrode is made through a hole in the bottom of the holder.

The initial attempts at DEH testing of slip-impregnated pellets indicated that the rapid vaporization of the retained water and the organic compounds in the slip generated forces sufficient to dislodge pellet fragments and crack the quartz tube. A slow heating schedule was developed to prevent disruption of the pellet stack by ensuring that the volatilization of retained water and organic compounds is a gradual process. The line heater, located outside the specimen chamber, heats the specimen through the front window of the chamber. During an ∿90-min period of the preheat schedule, the specimen temperature is raised from ambient to ∿300°C as measured by the fuel-surface thermocouple. The 300°C temperature is maintained for an additional 30 min. This temperature is sufficient to volatilize the water and organics, but is low enough to prevent thermal decomposition of the organics and movement of fission gas.

3. Calculation of Transient Temperature History

An important part of the analysis of the DEH test results is the calculation of the transient temperature history. The computer code DEHTTD is used for this calculation. In DEHTTD, the transient heat-flow equation is solved based on measured values of voltage, current, and surface temperature, and literature values for the electrical conductivity, thermal conductivity, and heat capacity of UO_2. The output of the code consists of fuel temperature

as a function of pellet radius and transient time. The calculational procedure used to solve systems of ordinary differential equations was changed during the investigation to improve computational accuracy. The version of the code[27] used for the results presented in this report is based on the GEAR package of computer subroutines.[28] The accuracy of the code was checked by comparing calculated versus measured values of melt radii for tests in which central melting occurred. Good agreement was obtained for all tests.

Early in the development of DEHTTD, the need to account for the effect of fuel microcracking on thermal conductivity was recognized. For the calculations presented herein, the thermal conductivity value was reduced by an amount proportional to the extent of transient microcracking. The rationale behind this decision and a description of the model employed are discussed in Appendix A.

B. Irradiated Fuel Materials

With one exception, fuel from H. B. Robinson No. 2, a Westinghouse commercial pressurized-water reactor (PWR), was used for the DEH tests. A single test was performed on a specimen irradiated in the Saxton reactor, a Westinghouse experimental PWR.

The H. B. Robinson fuel, fabricated by Westinghouse, had an initial pellet density of 92% of theoretical and an initial ^{235}U enrichment of 2.55 wt. %. The fuel pellets were 15 mm long and 9.32 mm in diameter and had dished ends. Fuel from three rods taken from a 15 x 15 bundle were used for the DEH tests. The bundle was irradiated for two reactor cycles; the average linear heat generation rates (LHGR) were 22.4 and 17.7 kW/m for the first and second cycles, respectively. The ratio of peak-to-average LHGR was ∿1.3 to 1. The rods used in the present experiments were located in the assembly positions farthest away from control rods and instrumentation thimbles in order to avoid local distortions in the neutron flux. A typical axial profile of gross gamma activity of one of the three rods is shown in Fig. 8. The profile is nearly flat over the central 2.2 m of the 3.66-m-long fuel zone. The regularly spaced depressions in the profile are the result of localized low neutron fluxes at the positions of assembly grid plates. DEH test specimens were obtained from the central plateau, except for one specimen taken from near the rod end to check for burnup effects on transient fission-gas release.

Table II gives burnup analyses (as determined from mass-spectrometric measurements of ^{148}Nd) for three axial positions in one of the rods. Burnup values for fuel from other axial positions were estimated by normalizing the axial profile of gross gamma activity to a maximum burnup of 3.14 at. %.

TABLE II. Burnup Analysis of Robinson Rod F-7

Sample	Distance from Rod Bottom, m	U, g	^{148}Nd, g	Burnup, at. %
155AA8	0.006	2.9072	389.8	1.26
155AA7	0.57	2.0758	706.2	3.14
155AA3	0.93	1.9152	648.5	3.12

The fission-gas content of the fuel was determined by dissolving an ~9-g fuel specimen from the high-burnup central plateau and collecting the fission gas released by the dissolution. The fission gas generated and retained within the fuel during irradiation was determined to be 0.036 mmol of xenon per gram of fuel and 0.0024 mmol of krypton per gram of fuel. The measured pretest xenon and krypton concentrations were weighted according to the gamma activity profile shown in Fig. 8 to provide a normalization base for the transient gas release percentages given in Section III and Appendix B. The isotopic content of the retained gas is given in Table III.

TABLE III. Isotopic Analysis of Fission Gas in Robinson Fuel

Xenon			Krypton		
Isotope[a]	Concentration, %	Accuracy	Isotope	Concentration, %	Accuracy
128	0.03	±0.01	83	11.4	±0.3
130	0.14	±0.02	84	31.2	±0.4
131	8.0	±0.2	85	6.0	±0.3
132	20.5	±0.3	86	51.3	±0.3
134	28.1	±0.3			
136	43.3	±0.4			

[a]A detectable amount of an isotope of mass 129, possibly ^{129}I, was also present.

Fission-gas release during irradiation was determined to be ~0.2% on the basis of plenum-gas analysis.[29] Laser sampling[18] showed that the radial profile of retained fission gas in the irradiated fuel was essentially flat.

The Saxton fuel was also fabricated by Westinghouse. The dished-end pellets were 15 mm long and 8.53 mm in diameter. The pellet density was 92% and the ^{235}U enrichment was 12.5%. The fuel experienced a load-following power history during which it accumulated an average burnup of 1.8% at an average power of 29.1 kW/m.[30]

The results of retained fission-gas determinations on the irradiated Saxton fuel indicate that the pretest gas content (per gram of fuel) of the DEH specimens was 0.0134 mmol xenon and 0.026 mmol krypton.[25] The fission-gas release during the Saxton irradiation was approximately 20% of the amount generated.

III. EXPERIMENTAL RESULTS

A. Fission-gas Release during PCM Tests

The PCM test program consisted of 23 DEH experiments that encompassed a range of heating rates, maximum temperatures, and radial constraint conditions. Test conditions and fission-gas release values for the tests are listed in Appendix B.

1. Empirical Fission-gas Release Correlation

The temperature history for a typical PCM transient was described in Section I. This relatively complex behavior was represented by a set of simplified parameters for the purpose of developing empirical relationships between DEH transient temperature history and fission-gas release. A variety of temperature-history parameters were investigated as part of the analysis of the DEH test data. Not all temperature parameters were strongly correlated with fission-gas release. In particular, parameters that involve an integral of temperature over time were almost uncorrelated with fission-gas release. This result is shown in Fig. 9, a plot of xenon release against the time integral of fuel centerline temperature, $\int T_c(t)dt$.

Fission-gas release was found to be strongly correlated with the maximum temperature attained by the fuel during the transient and with the fuel centerline heating rate. The use of maximum volume-averaged temperature gradient as an alternate to maximum centerline temperature was also investigated. As shown in Fig. 1, a strong coupling exists between centerline temperature and radial temperature gradient for PCM thermal conditions. In addition, centerline temperature and volume-averaged radial temperature gradient reach their respective maximum values at nearly the same instant during the transient. The relationship between maximum centerline temperature, T_{cm}, and maximum volume-averaged radial temperature gradient, $(dT/dR)_m$, during the DEH simulations of PCM conditions is shown in Fig. 10. Data for all tests in which fuel melting did not occur are included in this figure.

The existence of a strong relationship between $(dT/dR)_m$ and T_{cm} proved to be an advantage in the development of empirical gas-release correlations. The choice of the parameter to be used in a particular application is largely a

matter of convenience. For tests in which fuel melting did not occur, T_{cm} is usually preferable because it can be accurately calculated and compared with calculated or measured temperatures from other experiments. For tests in which central fuel melting occurs, the calculated centerline temperature is expected to be erroneous because the geometry changes in the liquid zone are not modeled in the temperature calculation code. However, the radial temperature gradient in the unmelted peripheral fuel can still be accurately estimated. Therefore, the use of $(dT/dR)_m$ is preferred to describe tests in which melting occurs and to compare data from such tests with those in which the fuel remains unmelted.

In order to convert from T_{cm} to $(dT/dR)_m$ or vice versa, the data in Fig. 10 were fitted to a power law:

$$(dT/dR)_m = 1.46 \times 10^{-4} \times T_{cm}^{1.82}, \quad (1)$$

where T_{cm} is in K and $(dT/dR)_m$ is in K/mm.

Because central melt zones formed in 12 of the 23 DEH tests, $(dT/dR)_m$ was used in the development of the gas-release correlation as a means of including all tests. For cases in which melting does not occur, the correlation can be recast in terms of T_{cm} by using the substitution indicated in Eq. (1).

Modifications were made to the fission-gas release values and the heating rates of tests in which central melting occurred to maintain consistency with the evaluation of $(dT/dR)_m$ for unmelted regions only. The heating rate was calculated at the centerline for tests in which the fuel remained unmelted, and at a radial position corresponding to the maximum extent of melting for tests in which melting occurred. For example, if melting occurred out to a fractional radius of 0.2, the time-averaged heating rate at the 0.2 position was used in the correlation. In the balance of this report, (dT/dt) represents the time-averaged centerline heating rate in K/s for tests in which melting did not occur, and the time-averaged heating rate at the maximum melt radius for tests in which melting did occur. Fission-gas release was calculated for the unmelted regions of the specimen by assuming that all fission gas was released from the central melt zone. (This assumption is justified by the laser sampling studies described in Section III.A.2.) To summarize, all the parameters used in the correlations refer to the unmelted portions of the test specimens.

As a preliminary to developing the correlations, graphs of fission-gas release as a function of the temperature parameters were prepared to indicate the characteristics that the mathematical correlation would have to possess. Figure 11 shows a plot of fission-gas release as a function of $(dT/dR)_m$ for unconstrained specimens. This figure indicates that fission-gas release increases rapidly with increasing radial temperature gradient, and that for a given temperature gradient, a high heating rate produces less fission-gas release than a low heating rate.

The general form selected for the empirical correlation was that of a power law, i.e.,

$$Z = a_o \, (dT/dR)_m^{a_1} \, (dT/dt)^{a_2}, \quad (2)$$

where Z is the calculated precent fission-gas release, and a_o, a_1, and a_2 are constants determined by a multiple linear regression analysis of ln (gas release) against ln $(dT/dR)_m$ and ln (dT/dt). The results of the regression analysis for unconstrained tests are

$$a_o = 7.68 \times 10^{-7},$$
$$a_1 = 3.13,$$
$$a_2 = -0.346,$$

and

r (correlation coefficient) = 0.98;

that is,

$$Z_u = 7.68 \times 10^{-7} (dT/dR)_m^{3.13} (dT/dt)^{-0.346}, \quad (3)$$

where Z_u is the calculated fission-gas release from unconstrained fuel. Note that Z_u shows the required strong positive dependence on $(dT/dR)_m$ and negative dependence on (dT/dt). By substituting Eq. (1) into Eq. (3), the correlation can be written in terms of T_{cm}:

$$Z_i = 7.58 \times 10^{-19} T_{cm}^{5.70} \times (dT/dt)^{-0.346}. \quad (4)$$

The use of Eq. (4) is restricted to transients in which T_{cm} remains below melting.

A graph of Z, the calculated fission-gas release, as a function of the experimentally measured release values is given in Fig. 12. The solid line with a slope of 1 is the line of perfect agreement. The dashed lines above and below the solid line indicate deviations from perfect agreement by factors of +3/2 and -2/3, respectively. The open circles, which represent unconstrained tests, are generally within these limits.

The range of experimental conditions over which the correlation was determined is listed in Table IV. Although the correlation can be used outside this range, caution must be exercised when doing so. Errors are most likely for cases where $(dT/dR)_m$ or (dT/dt) approach zero. In the former case $Z_u \to 0$, which is unrealistic for transient heating, while in the latter case $Z_u \to \infty$, which is clearly impossible. As described in Section III.C below, the maximum temperature version of the correlation can be applied to LOCA conditions, in which the radial tempertaure gradient is 20 K/mm or less. This application represents a major extension of the useful range of the correlation. This correlation will probably give usable estimates of gas release for (dT/dt) values of as little as 1 K/s. However, information to support the use of the correlation for transients with heating rates in this range is unavailable at present.

To illustrate the effects of constraint on transient fission-gas release, the correlation described above was used to predict gas release for the constraint tests. These results are given by the filled circles in Fig. 12. The parameter Z_u overpredicts fission-gas release for the constraint tests by an average factor of 3.76. Because of the small data set, no attempt was made to determine the multiple variable regression equation for the unconstrained tests. However, the data can be adequately described by a straight line lying

parallel to and above the regression line for unconstrained tests, as shown in Fig. 12. Therefore, a reasonable estimate for Z_c, the transient fission-gas release from constrained fuel specimens, is

$$Z_c = 2.04 \times 10^{-7} \, (dT/dR)_m^{3.13} \, (dT/dt)^{-0.346} \quad (5)$$

or

$$Z_c = 2.02 \times 10^{-19} \, T_{cm}^{5.70} \, (dT/dt)^{-0.346}. \quad (6)$$

TABLE IV. Range of Verification of Empirical Gas-release Correlation

Material Variables	
Fuel burnup	1.5-3.1 at. %
Linear heat-generation rate	17-35 kW/m
Transient Conditions	
Time-averaged fuel centerline heating rate	5-300 K/s
Maximum volume-averaged fuel radial temperature gradient	80-550 K/mm
Time of transient	5-100 s

The strong dependence of transient fission-gas release on T_{cm} or $(dT/dR)_m$ means that the accuracy of the empirical-correlation predictions will be very sensitive to the accuracy of the transient-temperature calculations. The effect of errors in the calculated maximum centerline temperature on the predicted gas-release values is shown in Fig. 13. The errors in fission-gas release introduced by errors in T_{cm} of ±100 K are less than the uncertainties in the gas-release correlation, i.e. the factors of +3/2 and -2/3 shown in Fig. 12. The fractional error is largest for low-temperature transients, in which the absolute gas release is the smallest. Errors in heating rate have a much smaller effect on the predicted gas release because of the slow variation of Z with (dT/dt). An error of 50% in (dT/dt) leads to an error of only 13% in gas release.

The accuracy of the DEH temperature calculations could only be checked for those tests in which central melting occurred. Good agreement between the calculated and observed melt radii was obtained in all such cases. Based on this agreement, the average error in calculated maximum temperatures for tests in which the fuel did not melt is estimated to be ±50 K. The maximum error is estimated to be ±100 K. Therefore, the expected errors in the calculated temperatures lead to uncertainties in the predictions of the empirical correlation that are no larger than the scatter in the data.

2. Radial Profile of Fission-gas Release

The laser sampling technique[18] was used to determine the ^{85}Kr content of the test-33 fuel specimens. Fission-gas release as a function of radial position was determined by comparison of the pretest and posttest laser data. The radial profile of ^{85}Kr release for test 33 is shown in Fig. 14. As expected, almost all the gas was released from the central molten zone. Note,

however, that an equal amount of gas was released from the unmelted fuel immediately adjacent to the melt. In the remainder of the specimen, a smooth decrease in fractional release was observed with increasing fractional radius.

B. Transient-Induced Microstructural Changes

During the DEH transients, intergranular fission-gas bubbles formed, grew, and coalesced, thereby producing interlinked tunnels on the grain faces and edges. In addition, microcracks formed in response to applied and differential thermal expansion stresses, and propagated along the weakened grain boundaries. The tunnels and microcracks were instrumental in venting fission gas that migrated from the grain interiors to the grain boundaries. This section contains a description of the microstructural changes and their relationship to fission-gas release.

1. Description of Pretest Microstructure

During irradiation, the density of the Robinson fuel increased from the as-fabricated value of 92% to a final density of 94% of theoretical. Approximately half the porosity in the irradiated fuel is in the form of large, roughly spherical pores with diameters in the range 0.03-0.25 mm. These pores, formed during fabrication, were apparently not altered during irradiation. Examples of this kind of porosity are visible in Fig. 15, a polished plane section through an as-irradiated fuel pellet. Most of the remaining porosity consists of isolated intergranular pores that are too small to be visible at the magnification of Fig. 15. These pores range in size from 0.5 to 2.0 μm and have a specific surface area of 69 mm^2/mm^3. The fine-scale pores are remnants of the as-fabricated porosity after in-reactor densification.

Intra- and intergranular fission-gas bubbles with diameters between 10 and 20 nm were also present in the as-irradiated structure. The total density of fission-gas bubbles, determined from replica fractographs of the type shown in Fig. 16, was $\sim 10^{10}$ to 10^{11} bubbles/mm^3.

The microstructure of the as-irradiated Saxton fuel was similar to that of the Robinson fuel, with one exception: The higher-power operation of the Saxton fuel produced a central region of large grains and interlinked porosity, as shown in Figs. 17 and 18. The central zone extends from the center to a fractional pellet radius of ~0.6. The grain size as measured by the mean linear intercept method is 10-12 μm in the central zone. A detailed description of the Saxton fuel microstructure is contained in Ref. 25.

2. Qualitative Description of Transient Microstructural Changes

The early stages of transient microstructural evolution were studied by examining fuel fracture surfaces in the scanning electron microscope (SEM). The surfaces were prepared by fracturing specimens at room temperature after DEH testing. For the operating conditions of the present study, the SEM has an effective resolution limit of ~35 nm.

The following description of transient-induced microstructural changes begins when the bubbles first become visible.

The first detectable event is the motion of fission gas from the grain interiors to the grain boundaries, where the gas collects in bubbles. Figure 19 shows this effect in a peripheral region of the specimen from DEH test 24. The fracture mode is mixed, i.e., partly transgranular and partly intergranular. This region of fuel experienced a maximum temperature of 1680 K. The density of bubbles larger than 35 nm is $\sim 10^{10}/mm^3$. A comparison with Fig. 16 shows that the size of grain-boundary bubbles increased dramatically while the number density remained roughly constant during the transient.

With continued heating, the grain-surface bubbles grow and coalesce. When two bubbles of less than a critical size coalesce, the resultant bubble quickly assumes a circular lens shape, i.e., an equilibrium bubble shape although not necessarily an equilibrium size. Once the bubbles reach a critical size, further coalescence results first in rod-shaped bubbles, and then in sinuous interconnected channels. Both these effects are illustrated in Fig. 20, which shows another area of the test-24 fuel, in this case heated to a maximum temperature of $\sim$1770 K. The bubble growth and coalescence processes have progressed to different stages on the various grain faces. However, all of the bubbles on an individual grain face have evolved to essentially the same stage. Note particularly that some grain faces containing well-developed interconnected channels are adjacent to grain faces containing isolated bubbles.

With continued heating, further channel formation occurs. In addition, tunnels form and grow along the grain edges. The grain-edge tunnels are prominent in Fig. 21, which shows the test-24 fuel structure at a location that reached a temperature of 1870 K. When interlinked for sufficiently long distances through the structure, these tunnels can vent fission gas that is able to reach the boundary.

The sequence of structures just described was observed to form at centerline heating rates of 10 to 50 K/s. At high heating rates, evolution of intergranular bubble structures followed a somewhat different course. Structures representative of heating rates of 25 and 300 K/s are compared in Fig. 22. At the higher heating rate, the critical bubble size for grain-surface channel formation is smaller. The width of the channels, which approximates the critical bubble diameter, is reduced by roughly a factor of 2 for a tenfold increase in heating rate. A second structural difference is the almost total absence of grain-edge tunnels at the higher heating rate. An "embryonic" tunnel is visible along one of the grain edges in the 300 K/s structure; this is one of the few observed instances of edge-tunnel formation at a high heating rate. Clearly, the interlinkage of edge tunnels made a negligible contribution to fission-gas release in this case. However, extensive microcracking occurred during the high-heating-rate tests. As described below, intergranular microcracking is believed to have been the primary fission-gas release mechanism in these tests.

The second significant microstructural change that occurs during transient heating is intergranular microcracking. On the SEM fractographs, where the microcracks are nearly perpendicular to the fracture surface, they appear as separations between adjacent grains; where they intersect the fracture surface at a glancing angle, they appear as dark, relatively featureless grains. Examples of the latter situation can be seen on the left

featureless grains. Examples of the latter situation can be seen on the left side of Fig. 2. The surfaces are featureless in the sense that no remnants of the bubble/channel structure remains. However, the microcracks are characterized by smoothly undulating surfaces with sharp changes in direction at grain edges. The microcrack surfaces are very similar in appearance to UO_2 and mixed-oxide grain surfaces that have been deformed by grain-boundary sliding.[31]

The appearance of the microcracks on a polished section is shown in Fig. 23. The intergranular nature of the cracks is apparent. The extent of cracking, as measured by the fraction of the grain surface area occupied by cracks, is quite large. In addition, the cracks are preferentially oriented, with the predominant orientation running from upper left to lower right in the photograph. Preferred orientation was observed in roughly 50% of the areas that had microcracks.

The general pattern of microcracking observed in the DEH-tested fuel specimens is schematically illustrated in Fig. 24. Near the center of the fuel pellet, the microcracks are randomly oriented. As distance from the center increases, the microcracks begin to exhibit preferential orientation, with the cracks aligned perpendicular to the pellet radius. The orientation direction tends to curve outward in the vicinity of the preexisting macrocracks. The extent of preferred orientation peaks at a fractional radius of 0.5 to 0.6. At greater distances from the center, both the degree of orientation and the extent of microcracking decrease. The degree of preferential orientation could be determined from the intercept count, by taking the ratio of intercept counts measured perpendicular and parallel to the orientation direction. The degree of orientation was seldom found to exceed 2:1.

The density of microcracks was found to increase in the vicinity of obvious stress intensifiers, such as large pores and contact points between adjacent fuel particles. This result, coupled with the overall orientation pattern, suggests that both externally applied stresses and differential thermal expansion stresses are involved in the formation of microcracks. (Further supporting evidence for this conclusion is presented below in the description of mechanical constraint effects.) However, it is also clear that fission gas plays a role in the formation of microcracks. This point is illustrated in Fig. 25, a posttest longitudinal section through the interface of an irradiated fuel pellet (top) and an unirradiated, depleted UO_2 spacer pellet (bottom). The white line at the interface is a sintered layer of molybdenum powder, which was applied to promote good electrical contact between the pellets. The fuel and spacer pellet experienced nearly identical thermal histories during the transient, and the stress states were correspondingly similar. Note that melt zones formed in both the irradiated and unirradiated material. However, microcracking occurred only in the irradiated fuel, clearly indicating the role of fission products in the microcracking process.

Fission products, and in particular fission gases, appear to affect microcrack formation by one or both of the following mechanisms. First, the presence of intergranular gas bubbles can drastically reduce the load-bearing area of grain boundaries and thus promote intergranular crack propagation under the action of applied stress. Second, during transient heating, the

pressure required to balance surface tension because mechanical equilibrium has not been achieved. The internal pressure may be sufficient to cause the grain boundaries to separate. The relative balance between these mechanisms is a complex function of stress state, temperature, bubble pressurization, and heating rate.

The propagation of microcracks can lead to their interconnection over long distances through the structure, and thus provide additional pathways for fission-gas release. The relative importance of microcracking and tunnel interlinkage as gas-release mechanisms is discussed in Section III.B.3 below.

A second class of intergranular separations was generally observed in the hotter portions of the specimen. Regions with these separations exhibit the morphology commonly attributed to isotropic intergranular swelling. Figure 26 shows this structure in the test-41 fuel. Note that the separations are generally planar, although the tips of the separations are rounded. Bubbles or channels with circular and oval cross sections are also present. These features allow the swelling morphology to be distinguished from microcracks in most cases. However, the differences between the two structures are relatively slight. The close similarity suggests that the swelling morphology may arise from microcracks by surface-rounding processes.

The high areal coverage of grain surfaces by pores in Fig. 26 indicates that interlinkage of the intergranular porosity, and consequent fission-gas release, has occurred. Because microcracks and isotropic intergranular swelling are so similar in form and function, the term "intergranular separations" is used to refer to both morphologies.

In 12 of the 23 DEH tests, the central portion of the fuel column was heated above the melting point. The resulting circular melt zones were usually slightly off of the fuel centerline, indicating that the heating profiles were not perfectly centrosymmetric. The radii of melting for the DEH tests are indicated in Appendix B. For H. B. Robinson specimens, the fuel within the melt zone contained large, distended pores, as shown in Fig. 27. The pores are largest at the center of the melt zone and gradually decrease in size as the outer edge of the melt zone is approached. Near the edge, the pore size approaches that of the intergranular pores in the unmelted fuel. For this reason, the boundary between melted and unmelted material is difficult to locate with precision.

In contrast, the boundary of the melt zone in the DEH-tested Saxton fuel, shown in Fig. 28, is sharply defined. Very little porosity is present in the melt zone. The solidification structure is apparent, with columnar grains and a small amount of shrinkage voiding clearly visible. The difference in appearance of the melt zones of the Robinson and Saxton fuels is due to the low pretest fission-gas concentration in the central region of the Saxton fuel,[25] which experienced high fuel temperatures during irradiation.[30]

3. Quantitative Description of Transient Microstructural Changes

The development of intergranular separations was characterized quantitatively by stereology measurements of their volume fraction, V_v, and surface area per unit volume, S_v. The early stages of channel and tunnel formation could not be reliably resolved on the 250X micrographs used for

these measurements. However, the contribution of channels and tunnels to the overall swelling was small, so very little error was introduced by this systematic bias. Once the channels reached a diameter of roughly 0.3 μm, no difficulty was experienced in their measurement.

Radial profiles of V_v and S_v were determined from measurements on a transverse section near the midplane of the DEH-tested fuel pellets. The profiles were used to calculate volume-averaged values of V_v and S_v, assuming that no axial variations in microstructure were present. Owing to the effects of macrocracks and large pores described above, significant azimuthal variations in the density of microcracks were sometimes observed. Such variations were accounted for by taking weighted averages of V_v and S_v in the affected and unaffected areas.

Typically, the volume fraction and surface area were highest at the fuel centerline, or in the hottest unmelted fuel region for specimens in which central melting occurred, and decreased with increasing distance from the center. An exception to this pattern was observed in specimens from long-time, high-temperature tests, e.g., tests 26 and 33. In these specimens, significant surface rounding occurred in the fuel just outside the melt zone. As a result, S_v is highest at an intermediate radial position. The monotonic decrease and intermediate maximum types of behavior are illustrated in Figs. 29 and 30. Note that the intermediate maximum is observed only in S_v, and not in V_v.

The radial profiles of V_v and S_v for radially constrained specimens exhibit a distinctive behavior, as shown in Figs. 29 and 30. The pore surface area in the test-44 specimen, for example, is nearly constant from the edge of the melt zone to a radius of 0.64, at which point it drops discontinuously to essentially the pretest value. Although surface area is constant within the affected zone, the pattern of microcrack orientation is not. Just inside the boundary of the affected zone, the microcracks are oriented circumferentially, while random orientation is observed closer to the melt zone.

One important result of the quantitative study of microstructure is that the path of microstructural change is essentially the same during the early stages of all the PCM simulations. By "path of microstructural change" is meant the transient-induced sequence of microstructural states as given by the S_v and V_v values. The common path can be illustrated by plotting S_v as a function of V_v for all DEH-tested specimens, as in Fig. 31. Each data point in this figure is an azimuthal average at a single fractional radius in a single test. Although some scatter is evident, the data for a relatively wide range of transient conditions can be described on one curve. Note in particular that the application of radial constraint does not affect the relationship between S_v and V_v. The best-fit equation of the curve in Fig. 30 is $S_v = 1.42 \times 10^3 \, V_v^{0.8146}$.

The path of microstructural change described not only the extent of microcracking, but also the average width of the microcracks, as given (approximately) by the parameter $2 V_v/S_v$. As shown in Fig. 31, the crack width increases slightly during the transients. However, the most important microstructural process shown in this figure is the increase in microcrack length.

The surface rounding that occurred in the hottest unmelted fuel in some transients produces a large decrease in S_v with little change in V_v (see Figs. 26 and 30). Surface rounding of this degree represents a significant departure from the path of microstructural change described above. Extreme surface rounding, such as that in Fig. 26, was only observed in fuel that was heated almost to melting for periods of 10 s or longer. The quantitative stereology measurements of zones in which extreme surface rounding occurred were excluded from Fig. 31 so that the effects of microcracking could be seen easily.

4. Empirical Relationship between Fission-gas Release and Microstructural Change

If the microstructural changes described above are involved in the release of fission gases to the extent implied in the preceding discussions, relationships should appear between fission-gas release and the extent of microstructural change as measured by the quantitative stereology parameters. To test this hypothesis, gas release was plotted as a function of volume-averaged values of V_v, as shown in Fig. 32. (Because of the strong, and nearly linear, relationship between V_v and S_v, an almost identical graph is obtained by plotting gas release versus S_v.) Recall that the pretest value of V_v was 0.03. The total pore volume fraction, including the initial contribution of 0.03, is plotted in Fig. 32.

First, consider the behavior of unconstrained specimens at low heating rates. Fission-gas release increases steadily with increasing pore volume fraction until a xenon release of $\sim$13% is reached at $V_v \tilde{=} 0.17$. For higher pore volume fractions, a much more rapid increase in gas release occurs, as xenon release reaches 60% for $V_v \tilde{=} 0.27$.

The filled circles in Fig. 31 show the behavior of radially constrained specimens. These data are in good agreement with the initial portion of the curve for unconstrained tests. However, none of the constraint tests reached the high-slope region of the curve. This is so even though the thermal conditions in several of the constraint tests were similar to those of unconstrained tests on the high-slope portion. The lower fission-gas release from constrained relative to unconstrained specimens tested under equivalent conditions was discussed in Section III.A.1. Figure 32 makes a stronger statement about the effects of constraint: The fission-gas release from a constrained specimen corresponds closely to the release that would be expected from an unconstrained specimen with an equivalent amount of intergranular separation. This result demonstrates the important role of intergranular separations in fission-gas release.

The relationship between gas release and V_v in the high-heating-rate tests appears to be somewhat different from that of the lower-heating-rate tests, although it is difficult to generalize from such a small data base. The data suggest that at high heating rates, little additional gas release occurs for volume fractions greater than 0.15. This result is consistent with the fact that at high heating rates, little time is available for the transport of fission gas to the grain boundaries. Hence, only a relatively small fraction of the total fission gas is available for release by an interlinkage mechanism.

C. Gas Release during LOCA Tests

Because of some limitations in the DEH test equipment, the temperature histories of the LOCA simulations departed somewhat from the LOCA history shown in Fig 2. Before presenting the results of the LOCA studies, the differences between the ideal case and the temperatures actually attained will be discussed.

The infrared pyrometer used for surface temperature measurement is sighted through the hot-cell window. Because of the attenuation of infrared radiation by the window, the pyrometer cannot measure temperatures below 1300 K. Therefore, the fuel surface temperature must be kept at a relatively high value in order to get usable temperature readings. In the case of the LOCA simulations, this restriction made it impossible to simulate the drop in centerline tempertaure corresponding to loss of moderator at the start of the transient. The temperature history actually achieved during the LOCA simulations is shown in Fig. 33. Note that the temperature difference between center and surface decreased during the first 14 s of the test, and then remained roughly constant. The average heating rates were 4.6 and 6.8 K/s at the center and surface, respectively. The volume-averaged radial temperature gradient was 80.8 K/mm at the start of the test and 63.1 K/mm at the end. This behavior differs considerably from the PCM simulations, in which center temperature increased much more rapidly than surface temperature. In general, the DEH LOCA tests achieved higher temperatures and higher temperature gradients than were desired.

These differences act in the direction of producing higher gas release in the DEH test than in a design-basis LOCA. In this regard, note that the rapid initial drop in centerline temperature, missing in the DEH test, is comparable to what would occur during an operational scram, and therefore makes a negligible contribution to fission-gas release. Apparently then, the DEH "simulations" of LOCA conditions should provide an upper bound on LOCA gas release.

Two LOCA simulations were performed as part of the present study. The thermal history of the second test was similar to that shown in Fig. 33. (See Appendix B for a summary of test conditions.) Xenon release was 1.2 and 0.2% for tests 48 and 53, respectively. Posttest characterization revealed that transient-induced microstructural changes were limited to the formation of a few fission-gas bubbles on grain boundaries, as shown in Fig. 34. Neither tunnel interlinkage nor microcracking occurred.

The results suggest that fission-gas release during the refill portion of a LOCA will be approximately 1%, and thus will have a relatively small effect on the further development of the accident sequence.

The empirical correlations originally developed for the description of fission-gas release during PCM conditions were tested against the LOCA simulation data to determine the applicability of the correlations outside the range of the development data base. For the LOCA applications, the maximum-temperature version of the correlation, i.e., Eq. (4), was used. Note that the centerline temperature is not strongly coupled to the radial temperature gradient during the LOCA tests. The maximum-temperature version of the correlation gives higher predicted gas-release values for LOCA tests than the

maximum radial temperature gradient version does. The maximum-temperature version will, therefore, give a more conservative estimate of LOCA gas release.

The results of the comparison are summarized in Table V.

Table V

Application of Empirical Gas-release Correlations to LOCA Conditions

	Test 48	Test 53	Design-basis LOCA
T_{cm}, K	1850	1850	1560
(dT/dt), K/s	4.9	3.5	4.4
Measured Gas Release, %	1.2	0.2	-
Predicted Gas Release, %	1.8	2.1	0.7

The empirical correlation gives gas-release predictions that are relatively small, but still exceed the measured values. The prediction for the design-basis LOCA is based on the temperature history shown in Fig. 2. The predicted fission-gas release is smaller for the design-basis LOCA than for either test 48 or 53, which is consistent with the inference that the DEH simulations of LOCA conditions were more severe than a design-basis LOCA.

The comparisons of Table V indicate that the maximum-temperature version of the empirical correlation can be used to estimate fission-gas release during design-basis LOCA conditions. The correlation is expected to give a conservative prediction of gas release during the refill and reflood portions of the transient.

IV. DISCUSSION OF RESULTS

A. Role of Microstructural Changes in Transient Fission-gas Release

The results of the DEH test program indicate that both grain-edge tunnels and planar intergranular separations occur during PCM-type transients and that both mechanisms contribute to the observed fission-gas-release fractions. In fact, sensitivity analyses performed with GRASS-SST indicate that in the absence of interlinkage mechanisms, fission-gas release would be no more than a few percent for any of the DEH tests.[14]

A qualitative picture of the relationships among the fission-gas-release processes during transient heating is presented in Fig. 35. Fission gas is transported to grain surfaces, where it collects in bubbles. Under the action of diffusional processes, the grain-surface bubbles grow and coalesce to form new lenticular bubbles. When the bubbles reach a critical size determined by temperature and heating rate, further coalescence results in rod-shaped

segments which quickly join to form sinuous channels on the grain surfaces. The channels can vent the contained fission gas to the grain edges, thus leading to the formation of stable grain-edge tunnels. Long-range interconnection of the tunnels vents fission gas to the exterior of the pellet. In addition, the venting of channels and tunnels reduces their internal pressurization and, given prolonged heating, may allow the grain-face channels to sinter closed. Figure 35 indicates that resintering completes the cycle of microstructural evolution and allows the sequence of bubble, channel, and tunnel formation to repeat.

Tunnel interlinkage is thus seen to be the end result of processes that always occur in a fixed sequence. However, microcracking can interrupt this sequential process at any stage and lead to large gas-release fractions. Microcracking operates in parallel with tunnel interlinkage and is thus capable of circumventing "blocked" steps in the tunnel interlinkage sequence. For example, tunnels did not form on grain edges in high-heating-rate tests, as shown in Fig. 22. The observed gas relase in this test was, therefore, almost wholly the result of microcracking. In slow-heating-rate tests, sufficient time at elevated temperature is available for the development of edge tunnels. Therefore, at slow heating rates, a larger fraction of the released fission gas is thought to be due to tunnel interlinkage. However, microcracking occurred and presumably contributed to fission-gas release in almost all of the DEH tests.

In addition to this qualitative picture, quantitative data on transient gas release and microstructural change are available. These data make possible quantitative estimates of the relative contributions of tunnel interlinkage and microcracking to gas release. To make the estimates, it is first necessary to give a more detailed description of the observed dependence of gas release on microstructural change.

The quantitative stereology measurements of the surface area of intergranular separations can be used to determine the fraction of the original grain boundaries that separate during a transient. Fission-gas release is plotted as a function of the fraction of separated grain boundaries, denoted by α, in Fig. 36. Although this graph is similar to Fig. 31, some important differences are evident. First, for the sake of clarity, the data for high-heating-rate tests are omitted. Second, gas release and fractional separation in test 33 were plotted separately for each radial zone in the fuel. These data were obtained from the measured profile of ^{85}Kr release (Fig. 14), corrected for the different release fractions of Kr and Xe. The values of f and α for the remaining tests are volume averages.

The data in Fig. 36 fall naturally into two groups. For $\alpha < 0.4$, the data show considerable scatter about the line

$$f = 0.43\,\alpha, \tag{7}$$

where f is the fractional xenon release. For $\alpha > 0.4$, the data follow the relationship

$$f = \alpha, \tag{8}$$

with relatively little scatter.

The transition between the two types of behavior can be identified with the onset of long-range interconnection of planar intergranular separations or microcracks. This result is based on a percolation-theory[32] treatment of the problem, which predicts that long-range interconnection of microcracks occurs for $\alpha > 0.36$, which agrees with the observed transition at $\alpha \approx 0.4$.

A general result of percolation theory is that the transition between no interlinkage and extensive long-range interlinkage occurs almost discontinuously, if the interconnections are assumed to form randomly in space. In the present case, the separation of grain faces by microcracking is not a random process; new cracks tend to form at the tips of existing ones. For this reason, some long-range interconnection of microcracks occurred when the fraction of the grain-surface area occupied by microcracks was relatively low. Therefore, we would expect that a portion of the observed gas release in the low-α region is due to nonrandom interlinkage of microcracks. Most of the remaining gas release at low α is due to tunnel interlinkage, which can occur at volume fractions corresponding to $\alpha \approx 0.12$. The data scatter for low α values in Fig. 36 is probably due to varying degrees of microcrack and tunnel interlinkage in the different tests represented.

The data points for constrained specimens (filled circles in Fig. 36) all lie in the low-α regime, indicating that long-range microcrack interlinkage did not occur during the constraint tests. The fact that these data tend to lie below the data for the unconstrained tests at a given value of α is an indication that constraint may also inhibit tunnel interlinkage, which apparently was the major gas-release process in the low-α regime.

The relative absence of scatter in the data at high α values can also be explained as an interlinkage effect. Above the threshold for long-range interlinkage, nearly all the microcracked surfaces will be connected to the outside. Therefore, any incremental increases in the amount of microcracking will result in direct venting of the associated fission gas to the outside. This situation leads to a strong dependence of fission-gas release on the fractional separation of the grain-boundary area. Note that it is technically possible for fission gas to be released from a grain face by tunnel interlinkage before that grain face is opened by a microcrack. Further, the posttest examination can give no direct information as to whether tunnel interlinkage preceded microcracking on a particular grain face. However, the strong relationship between f and α implies that, in the high-α regime, gas was released when the microcracks formed, and that tunnel interlinkage prior to microcracking was minimal.

Figure 36 can also be used to estimate the amount of gas that was able to diffuse from the interior of the grains to the grain surface. Let g_s be the fraction of the total fission-gas content that reaches the grain surfaces either during prior irradiation or transient heating. Once long-range interlinkage occurs, the fraction of g_s that escapes by transient microcracking is given by α. Therefore, the total fractional fission-gas release, f, is given by

$$f = \alpha g_s. \tag{9}$$

Thus, when $f = \alpha$ (Fig. 36), $g_s = 1$. That is, for centerline heating rates of 100 K/s or less, all or nearly all of the fission gas is able to diffuse to the grain boundaries by the time interlinkage of the microcracks occurs.

At higher heating rates, as shown in Fig. 32, fission-gas release is much less sensitive to the extent of microcracking, even though the posttest microstructural examination revealed that microcracking was the predominant gas-release mechanism during these tests. The resolution of this apparent contradiction is that fission gas must be able to diffuse to the grain boundaries before it can be released via interconnected microcracks. Using the terminology introduced above, $g_s \ll 1$ for the high-heating-rate tests. In summary, for heating rates in excess of 200 K/s, gas release is controlled by the rate at which fission gas diffuses to the grain boundaries. In contrast, if the heating rate is less than 100 K/s, nearly all of the fission gas is able to diffuse to the grain surfaces before extensive microcracking occurs; under these conditions, gas release is controlled by microcracking.

B. Conditions Favoring Microcracking

The ability to determine whether microcracking will occur during a given thermal transient is an important element in the prediction of fission-gas release. In principle, a "classical" mechanical treatment, involving the high-temperature stress/strain relationships of UO_2, could be used to study microcracking. Not only is this approach very complex, but it would require knowledge of the mechanical properties of UO_2, including strain-rate effects, at high temperatures. Data in this area are sparse, and are almost nonexistent for temperatures in excess of 2400 K.

An alternate approach to modeling certain aspects of the mechanical behavior of oxide fuels has been developed by DiMelfi and Deitrich.[33] In their model, the growth of a grain-boundary bubble under the driving force of internal pressurization is studied. The volume growth rates due to crack propagation and diffusional processes are compared to determine the dominant mode of volume swelling. Knowledge of the mechanical properties of UO_2 is not required. The predictions of the model are in good agreement with the results of the DEH tests, as will be described in the following paragraphs. The model is limited to a prediction of whether microcracking or diffusion is the dominant mode of volume swelling. However, this information is important to the prediction of fission-gas release. In addition, the simplicity of the approach makes it an attractive alternative to a detailed mechanical analysis.

The underlying structure of the model can be summarized as follows. A lenticular fission-gas bubble on a grain boundary can be viewed as a crack nucleus. It can be shown that such a crack will propagate unstably if the internal pressure exceeds that required for bubble equilibrium, i.e., if

$$p > \frac{\gamma_s}{\rho} - \sigma, \qquad (10)$$

where p is the internal pressure, γ_s is the fuel-gas surface energy, ρ is the radius of curvature, and σ is the applied tensile stress normal to the boundary.

Further, if a grain-boundary bubble, initially at equilibrium, is subjected to transient heating, the internal pressure will increase above the equilibrium value. Under these conditions, crack propagation will occur unless diffusional growth of the bubble occurs rapidly enough to maintain equilibrium condtions.

During most thermal transients, the initial mode of intergranular swelling will be crack propagation. The cracked bubble may be able to reattain its equilibrium shape by diffusional transport of material along the grain boundary. However, if the heating rate is sufficiently high, repressurization of the bubble may lead to further crack propagation before equilibration can take place. Thus, the competition between diffusional growth and crack growth determines whether bubbles tend to remain isolated or rapidly become part of an interconnected network of microcracks.

In the DiMelfi-Deitrich analysis, the dominant mode of intergranular swelling is determined by comparing the rates of volume swelling due to crack propagation and diffusional growth. In practice, this is done by comparing the instantaneous value of the grain-boundary diffusion coefficient, D_g, with the minimum value needed to maintain bubble equilibrium, D_g^{min}. (The calculation of D_g^{min} is discussed in detail in Ref. 31.) If $D_g < D_g^{min}$, cracking dominates; this behavior is termed "brittle". If $D_g > D_g^{min}$, diffusional growth or "ductile" behavior dominates.

This model was applied to the DEH test data by calculating $w D_g$ and $w D_g^{min}$ as a function of time for each radial fuel position in each DEH test. Here w is the effective grain-boundary thickness. The product $w D_g$ is used in the analysis because w is not determined explicitly. The behavior of $w D_g$ and $w D_g^{min}$ at the fuel centerline of test 32 is shown in Fig. 37. As expected, crack propagation dominates during the first part of the transient. However, as indicated by the crossover of the two curves, ductile behavior is predicted from 48 s until the end of transient heating at 60 s. In contrast, Fig. 38 shows that brittle behavior is predicted for the entire 60-s transient at $R/R_o = 0.44$.

These results suggest that the model can be tested by comparing the predictions with the observed microstructures in the DEH-tested specimens. That is, the 12 s of ductile behavior in Fig. 37 should produce a detectable surface-rounding, i.e., blunting of the crack tips and isolated grain-boundary bubbles, while crack tips should remain sharply pointed for the case shown in Fig. 38. The brittle and ductile morphologies are illustrated in Figs. 23 and 26, respectively.

The results of a comparison of the model predictions with the DEH test data are shown in Fig. 39, in which the time required for the onset of ductile behavior is plotted against the total test time. Model predictions of ductile and brittle behavior lie, respectively, below and above the line passing through the origin with slope = 1. Observed ductile and brittle morphologies are indicated by open and filled symbols, respectively. The close agreement between the data and the model predictions is evident.

The power of the model is that it describes the competition between crack propagation and diffusional processes. This competition is an important part of a mechanical model of transient phenomena, but is not itself the model. One important limitation of the DiMelfi-Deitrich approach is the simplified treatment of applied stress. Stress is assumed to be constant during the transient, equal to zero for the unconstrained tests and a high value for constrained tests. In reality, stresses due to the applied axial load, dif-

ferential thermal expansion, and relative motion of the fuel chunks are always present. Stress levels vary with position in the specimen and as a function of time during the transient.

The changing stress patterns cause large-scale microcracking to occur after diffusional bubble and channel growth, as was inferred from the SEM examination of fracture surfaces. This behavior is the opposite of that predicted by the model, in which microcrack propagation dominates the initial stages of a transient. Even though changing stress patterns can invert the predicted order of events during the initial portion of a transient, the model is still capable of accurately describing the behavior in the latter stages of a transient. This situation is probably due to the fact that large-scale microcracking reduces stresses and stress gradients, thereby producing conditions closer to the model assumptions. Once this has happened, the microstructure may develop an overall ductile appearance, depending on temperature, heating rate, and the time remaining in the transient.

The limitations in the model of ductile/brittle response indicate that it would give a more accurate description of fuel behavior if integrated with a relatively sophisticated mechanical model. Such a project would be a valuable follow-on to the results described in this report.

C. Comparison with Fission-gas Release and Microstructural Changes during Nuclear-heating Transients

A detailed comparison of fission-gas release and fuel behavior under both nuclear and electrical heating conditions was conducted as part of the DEH program.[25] In this section, the results of the earlier study are summarized and updated.

The comparison of the effects of nuclear and electrical heating was undertaken to determine whether nuclear heating produced the same kind of microstructural changes and gas-release behavior observed in DEH tests. The investigation determined that nuclear heating and DEH produced similar microcrack structures and similar amounts of fission-gas release. The bubbles and channels on the grain surfaces were virtually identical for the two heating methods.

The results of the earlier report were based primarily on posttest characterization of the irradiated Saxton fuel[30] used in the PBF IE-1 test.[34] The PCM transient in the IE-1 test was terminated by rewetting the cladding, which had been operating in a film-boiling condition. The resulting thermal shock to the fuel produced microcracking (i.e., fuel shattering) above that which occurred during film boiling.[35] For this reason, the extent of microcracking in the IE-1 test was somewhat greater than in the DEH tests.

A microcrack pattern of the DEH tests more closely approximates the morphologies produced during a power transient in the Dresden-3 reactor.[36] A longitudinal section through the Dresden-3 fuel (see Fig. 40) reveals that the fuel has swelled into the dish volume at a pellet-pellet interface. The fuel swelling mode is intergranular microcracking. The decrease in the extent of microcracking with distance from the pellet interface confirms the finding that mechanical constraint inhibits microcracking.

At higher magnification, as shown in Fig. 41, the microcrack morphology of the Dresden-3 fuel is seen to closely duplicate the structures of the DEH-tested fuels. The only apparent difference in the structures shown in this figure is that of grain size. The bubbles and channels on grain boundaries shown in Fig. 42, in which microcracking did not occur, are similar to the structures observed in DEH- and PBF-tested fuels. From the standpoint of microstructure, the fission-gas-release mechanisms in the DEH tests and the Dresden transient are identical.

Although fission-gas-release measurements are not available for the Dresden-3 fuel rod, the results of this study can be used to give a rough estimate of transient fission-gas release. In the region around the pellet interfaces, approximately 50% of the grain boundaries are occupied by microcracks. With reference to Fig. 36, a 50% coverage of the grain boundaries corresponds to 50% fission-gas release, under the assumption that the fuel heating rates in the Dresden-3 transient fall within the envelope of PCM conditions explored in the DEH program. The 50% gas release applies only to the microcracked region. When averaged over the whole pellet volume, the gas release is $\sim$7.4%. (It should be noted that these estimates apply to a relatively low-power location, $\sim$30 cm from the base of the rod. The fission-gas release fraction may have been somewhat larger in high-power positions.) The relatively small overall gas release compared with the high value in the unconstrained portions of the fuel points up the important role of intact, undeformed cladding in holding fission-gas release to low levels during operational transients.

The DEH test results also have a potential application to the understanding of the TMI-2 accident sequence. The estimated core-wide release of ^{85}Kr during the TMI-2 accident is 70%,[37] implying that severe core damage has occurred. The physical processes that caused the damage and fission-gas release are likely to have involved breakup of the fuel into individual grains. Mechanical loads, fuel oxidation, and thermal shock are among the processes that may have contributed to fuel breakup. This picture of gas release during the TMI-2 accident is consistent with the results of the present study.

The DEH test results demonstrate that extensive microcracking can occur when the grain boundaries are weakened by the presence of fission-gas bubbles, particularly if cladding restraint is not present. On this basis, the TMI-2 fuel is expected to have been extremely vulnerable to fuel breakup.

Finally, note that the DEH technique offers a convenient means for studying fuel behavior during conditions typical of an uncovered core. If lengths of clad fuel were subjected to DEH in a high-temperature steam atmosphere, the electric current would flow mainly through the cladding. The ohmic heating of the cladding would heat the fuel indirectly, just as the exothermic oxidation of Zircaloy heated the fuel in TMI-2.[2] The similarity in heating profiles means that DEH is well suited for the study of fission-product release, fuel breakup, and UO_2-Zircaloy reaction under TMI-type conditions.

D. Licensing Considerations

Many of the DEH test program results are applicable to the types of transients analyzed in reactor licensing procedures. In this section, the potential application of the DEH test results to LOCAs, PCMs, rod-ejection accidents, and anticipated transients is discussed.

1. LOCA

The current licensing assumption for the design-basis LOCA is 25% release of iodine and 100% release of the noble gases.[3,4] The DEH tests reported in Section III.C indicate that only about 1% release will occur during the refill portions of a LOCA. Similary low release values have been calculated by the reactor vendors in their safety analyses.[1] Therefore, fission-gas release is expected to be of minimal consequence in a LOCA that is terminated by the successful operation of the ECCS.

In the case of a LOCA in which the core remains uncovered for an extended period (e.g., a TMI-type accident), the release of nearly all of the fission gas can be anticipated. The DEH tests demonstrated that more than 90% of the fission gas is released if the fuel melts, and that intergranular separations in unmelted fuel will under some circumstances produce release fractions that are nearly as high. Microcracking of the fuel is most pronounced in the absence of mechanical constraint, which would result from cladding ballooning. Fission-gas release would be highest under these conditions. Somewhat lower gas release values would be expected if the reactor cooling system pressure remained high while the core was uncovered. In this instance, the cladding would collapse on the fuel column and provide mechanical constraint. The DEH test results and the estimates of fission-gas release during the TMI-2 accident indicate that the current licensing assumptions are not overly conservative for the case of a degraded core.

Additional study of fission-product release and microcracking under conditions of severe core degradation is needed, with particular emphasis on the radiological consequences of various operator actions. However, since the fission-gas release fractions are known to be high for this class of accident, any new information that is developed would probaby have a minimal effect on licensing assumptions.

2. PCM

The broad class of PCM accidents includes transients with a wide variation in severity and a correspondingly wide range in expected fission-gas release. The topic of fission-gas release during PCMs is addressed during the licensing process, although the NRC has not issued specific licensing assumptions. However, the DEH test results are sufficiently detailed to be directly applied to calculations of gas release for a variety of PCM conditions.

Based on the DEH results, several important statements can be made regarding fission-gas release during a PCM transient:

(a) Because of the microcracking and tunnel interlinkage processes, a relatively large amount of fission gas can be released from fuel that does not exceed the melting point. Gas release can be conveniently described with an empirical correlation written in terms of the radial temperature gradient and the transient heating rate. Gas release was found to be proportional to $(dT/dR)_m^{3.13}$ and inversely proportional to $(dT/dt)^{0.346}$. The correlation can also be written in terms of maximum centerline temperature, in which case gas relaese is proportional to $T_{cm}^{5.70}$.

(b) Mechanical constraint reduces transient gas release by inhibiting the microcracking process. Transient gas release from constrained fuel was found to be less than that from unconstrained specimens tested under similar thermal conditions, by a factor of 3.76. This result means that an estimate of mechanical constraint is needed for an accurate prediction of fission-gas release. As an example, cladding creepdown or collapse provides a large degree of mechanical constraint and would restrict gas release for a given set of thermal conditions.

(c) The microcracking process reduces the effective fuel thermal conductivity, and thus leads to higher fuel temperatures and a larger fuel enthalpy than would be experienced in the absence of microcracking. Because thermal conductivity can be reduced by as much as a factor of 0.5, the effect on temperature and enthalpy can become significant in accidents where stored energy considerations are important.

(d) Nearly total release of fission gas can be expected from fuel that melts.

3. Rod-ejection Accident

In the Regulatory Guide treatment of the control-rod ejection accident, no specific allowance is made for the release of fission gas during the heatup phase of the transient prior to fuel melting. Instead, an assumption is made that accumulated gap inventory at the start of the transient is 10% of the total core inventory, and no further gas release occurs until fuel melting begins. This assumption should be reevaluated in light of the PCM simulations, which indicate the potential for appreciable fission-gas release from unmelted fuel.

A direct extrapolation of the DEH test results, obtained for maximum heating rates of 300 K/s, is not appropriate for the description of the rod-ejection accident, in which heating rates of several thousand degrees per second may occur. However, the trends established in the PCM simulations give important insights into the expected behavior at very high heating rates.

The decrease in gas release with increasing heating rate during the PCM simulations is ascribed to the short time available for the operation of diffusional processes. That is, very little fission gas is able to diffuse to the grain boundaries, and the tunnel interlinkage process is suppressed. In the limit of an extremely high heating rate, no diffusion will occur and microcracking or fuel shattering will be the only operative fission-gas release mechanism. Fuel shattering has, in fact, been observed in high-heating-rate transients.[38,39] Under these circumstances, only the fission gas already on the grain boundaries will be available for release from unmelted

fuel. The actual transient release will depend on the extent of microcracking and the amount of fission gas that accumulates on the grain boundaries during normal operation.

Although the grain-boundary fission-gas content can be calculated, e.g., by GRASS-SST,[14] it is a complex function of the reactor operating history. As an alternate, a new licensing assumption may be useful. To parallel the existing Regulatory Guide,[5] a revised assumption should account for both the amount of gas released to the gap during normal operation and the fission-gas content of the grain boundaries. The sum of these two terms will rarely be greater than 30% of the total core inventory. Therefore, a conservative assumption is that 30% of the fission gas is released from the fuel prior to melting. The conservatism of the assumption derives from the implication that all of the grain boundaries are opened by microcracking. Because of the severe fragmentation that has been observed in experimental studies,[38,39] the assumption is probably not overly conservative in this instance. The 30% figure can be supplanted by a direct calculation indicating that a smaller value is more realistic for a particular fuel design or reactor operating environment. Note that, because of the low probability and the relatively small amount of fuel involved in a rod ejection, the proposed guideline represents a small alteration in overall reactor safety.

4. Anticipated Transients

The American National Standards Institute (ANSI) defines a Condition II event as an incident of moderate frequency, with an expected occurrence of approximately one per reactor-year.[40] Licensing interest in such anticipated transients encompasses both the event itself and the question of safe operating limits in the aftermath of the transients. In the area of fission gas, the issue is usually taken to be whether the transient-induced gas release causes a significant reduction in gap conductance.

The milder transients among the PCM simulation series overlap the temperatures and heating rates typical of ANSI Condition II events. Therefore, the empirical correlation described in Section III.A.1 can be directly used for the prediction of gas release during these transients. The predictions of the correlation for typical thermal histories are shown in Fig. 43. In this figure, the maximum fuel temperature depicted is well below the melting point, reflecting the fact that fuel melting does not occur in this type of transient. Not all of the combinations of heating rate and maximum temperature indicated in the figure could actually be attained in an anticipated transient. For example, it is doubtful that a 10 K/s ramp would continue long enough for the fuel center temperature to reach 2900 K. However, even if this case is included, the fission-gas release predictions of the correlation are small.

Data from the DEH tests and in-reactor ramp tests[41,42] have been used by reactor vendors for their correlations of fission-gas release during Condition II events.[43,44] The vendor correlations indicate that fission-gas release during anticipated transients does not reduce gap conductance enough to raise fuel temperatures significantly.[43] However, no indication is given as to whether the effect of microcracking on thermal conductivity is considered.

The thermal conductivity correction factor can be relatively large, even for transients in which the fission-gas release is low. This point is illustrated by DEH test 42, in which a constrained specimen was heated to a calculated maximum center temperature of 2900 K at a heating rate of 53.1 K/s. These conditions are typical of a severe Condition II transient. The fission-gas release in test 42 was 2.2%. Because of microcracking, the thermal conductivity at the fuel centerline decreases during the transient to ~51% of the expected value. (See Appendix A for a discussion of the effect of microcracking on thermal conductivity.) If the correction to thermal conductivity is ignored, the calculated maximum temperature for test 42 is only 2390 K, i.e., 510 K less than the true value.

Current understanding of anticipated transients indicates that the expected gas release is low, and that the resulting effect on gap conductance is minimal. However transient-induced microcracking may lead to higher than expected temperatures during subsequent operation. Such microcracking may be confined to the regions adjacent to pellet interfaces, as in Fig. 40. Because of the potential effect on temperature calculations, microcracking should be included in analyses of Condition II events.

V. SUMMARY AND CONCLUSIONS

1. The DEH technique has been shown to be a useful method of simulating the thermal conditions typical of a variety of LWR transients. Fission-gas release can be readily studied because of the ease with which tests can be instrumented and released gases collected. The results of DEH tests can be directly applied to the estimation of fission-gas release during power transients.

2. Simulations of PCM conditions were used to develop a broadly applicable, empirical correlation for fission-gas release. Transient gas release was found to follow a relationship of the form

$$Z = k_1 (dT/dR)_m^{3.13} (dT/dt)^{-0.346},$$

where the constant k_1 is 7.68×10^{-7} for unconstrained fuel and 2.04×10^{-7} for constrained fuel. For transients in which no fuel melting occurs, the correlation can be written

$$Z = k_2 T_{cm}^{5.70} (dT/dt)^{-0.346}.$$

The constant $k_2 = 7.58 \times 10^{-19}$ for unconstrained fuel and 2.02×10^{-19} for constrained fuel.

3. The release of fission gas during transient heating was found to be controlled by the interlinkage of tunnels on grain edges and the formation of intergranular microcracks. Microcrack interlinkage ocurs when microcrack coverage of the grain boundaries exceeds 40%. Above this value, fractional fission-gas release is equal to the fraction of the grain surface area occupied by microcracks.

4. Mechanical constraint reduces fission-gas release by preventing the formation of microcracks. Therefore, transient gas release is strongly dependent on the loads at the fuel-cladding interface. For some operational transients, microcracking occurs only in the fuel adjacent to pellet interfaces, where swelling of fuel into the dish volume is possible.

5. A model of ductile/brittle fuel response[33] was found to give a good description of the microstructures produced by the PCM transients. The ductile/brittle response predictions can be incorporated into a detailed mechanical model of fuel behavior during thermal transients. The results of the DEH tests indicate that an integrated approach is needed for the description of transient fission-gas release and mechanical response.

6. The occurrence of microcracking during transient heating decreases the effective fuel thermal conductivity in proportion to the amount of microcracking. Locally, thermal conductivity can be reduced to less than half the expected value. The lower thermal conductivity can lead to significantly higher fuel temperatures both during the transient and in subsequent operation.

7. During the initial portion of a control-rod ejection accident, microcracking may lead to the release of a significant portion of the grain-boundary gas prior to fuel melting. To account for this effect in accident analyses, a reevaluation of the current licensing assumption is recommended. An assumed release of 30% of the fission gas prior to melting, rather than the existing 10%, appears to be more realistic. This change is expected to have a relatively small effect on overall reactor safety.

8. The PCM test results are directly applicable to the study of fission-gas release during ANSI Condition II events. Gas release during these transients is low, and the resulting effect on gap conductance is minimal. However, the potential for microcracking should be considered in calculating fuel temperatures during and after the transient.

9. DEH investigations of LOCA-like conditions indicate that fission-gas release during the refill portion of a design-basis LOCA will be 1% or less. The maximum-temperature version of the empirical correlation gives a conservative estimate of fission-gas release during a design-basis LOCA. For accidents that go beyond the design basis, microcracking, thermal shock, fuel chemical reactions, and fuel melting may occur. These processes can lead to the release of nearly all of the fission gas. Although the existing assumptions are very conservative for a design-basis LOCA, the conservatism for degraded-core conditions is not excessive. The DEH technique is well suited to the study of the initial stages of fuel breakup during prolonged core uncovery. Phenomena such as fission-product release, Zircaloy oxidation, clad ballooning and rupture, fuel-Zircaloy reactions, thermal shock, and mechanical loads can be investigated in appropriately designed DEH test equipment.

Acknowledgments. The support and encouragement of G. P. Marino of the NRC are gratefully acknowledged. At ANL L. A. Neimark and the staff of the Alpha-Gamma Hot Cell Facility assisted in all aspects of the program and J. Rest and L. R. Kelman provided many helpful discussions of the DEH technique and test results.

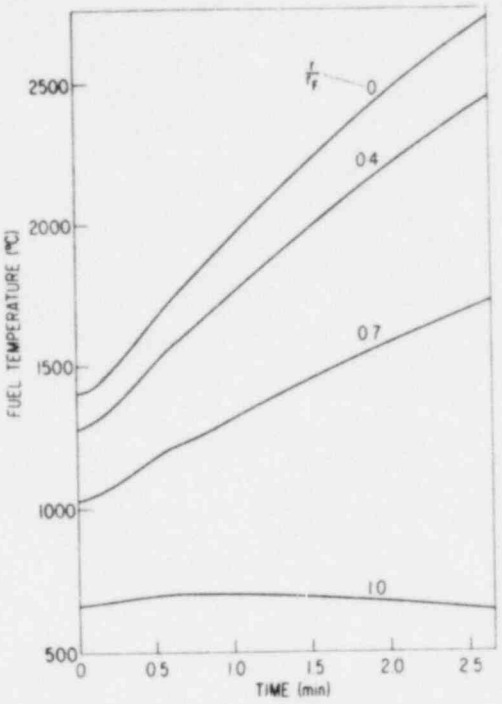

Fig. 1. Schematic Temperature History for a Typical PCM Accident Prior to Fuel Melting. ANL Neg. No. 306-77-567R1.

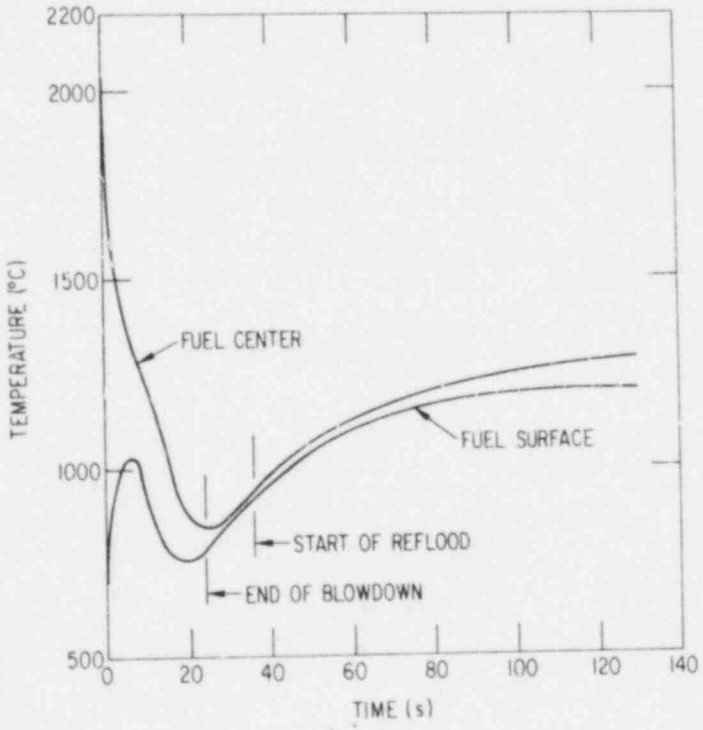

Fig. 2. Schematic Temperature History for the Blowdown and Refill Phases of a Cold Leg Break Double Offset LOCA. Neg. No. MSD-223965.

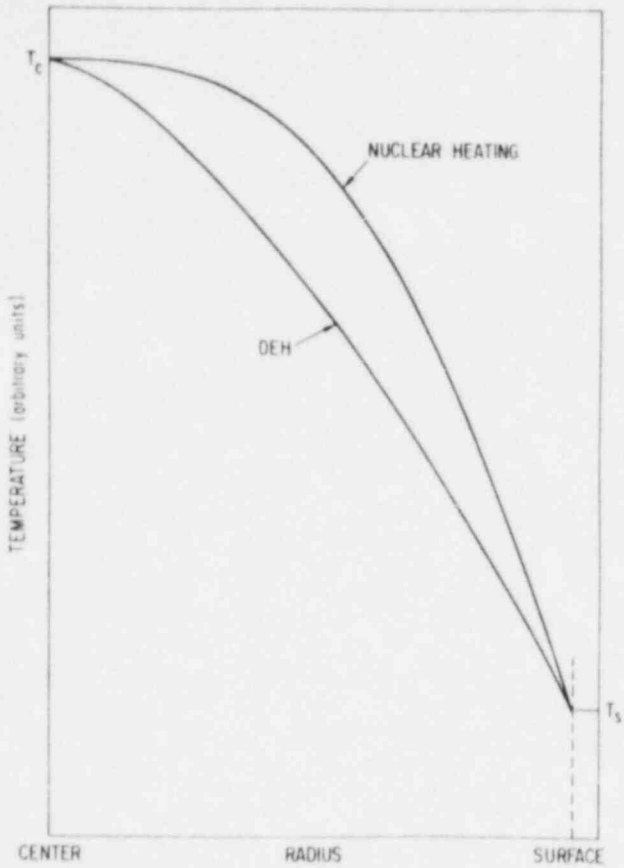

Fig. 3. Schematic Radial Temperature Profiles of Nuclear Heating and DEH. Neg. No. MSD-223528.

Fig. 4. The Original DEH Test Chamber and Associated Apparatus for Fission-gas Collection. ANL. Neg. No. 306-77-577.

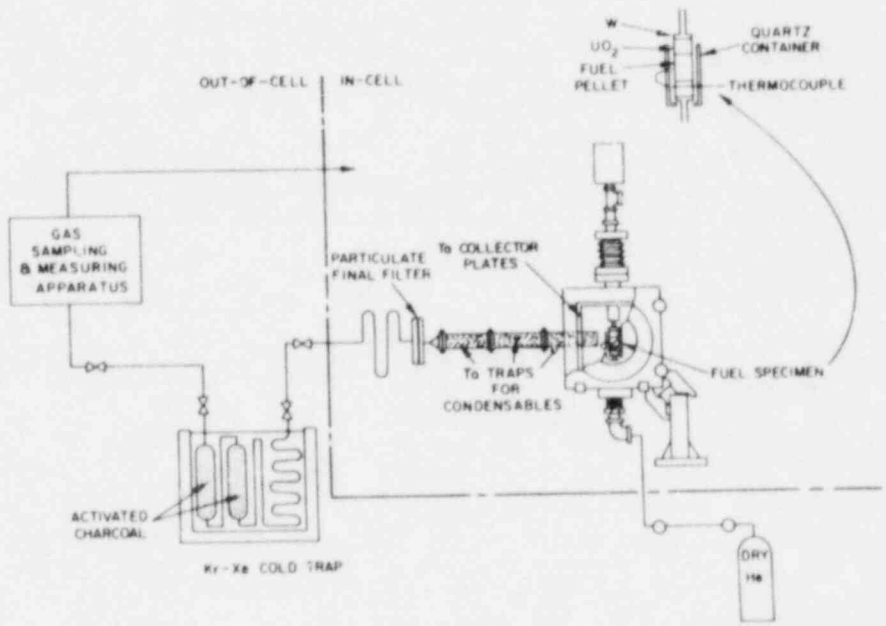

Schematic Design of In-cell DEH and Fission-product Collection Apparatus

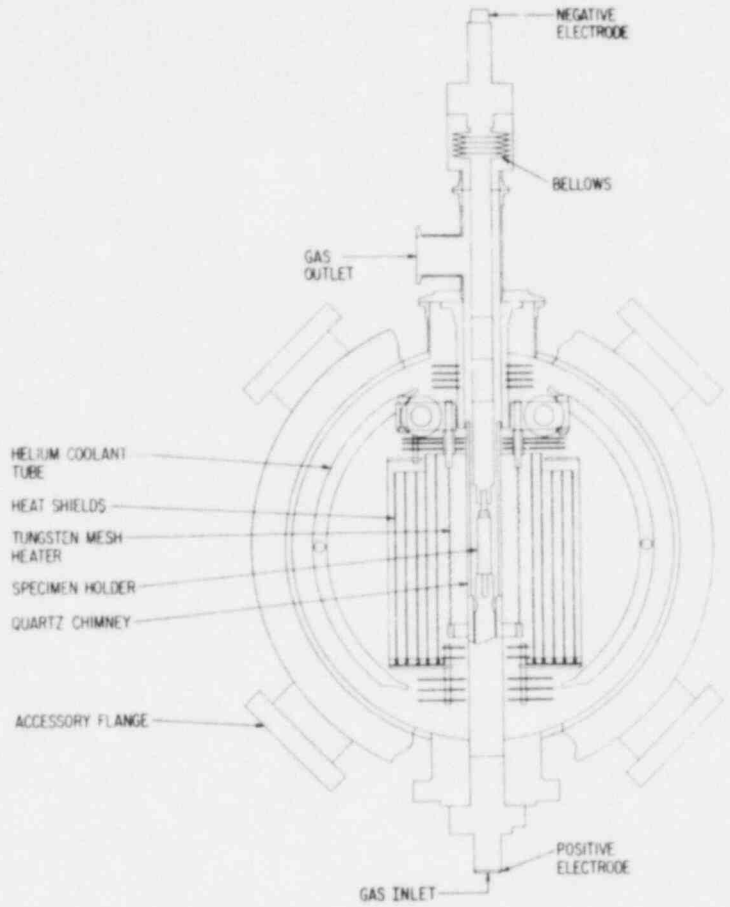

Fig. 5. The Second DEH Test Chamber. Neg. No. MSD-223740.

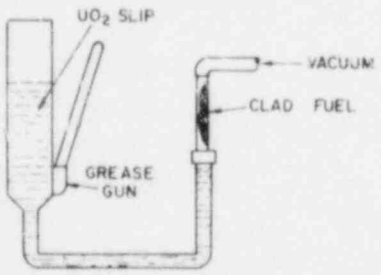

Fig. 6. Schematic of Apparatus for Impregnating Clad Lengths of Fuel with UO_2 Slip. Neg. No. MSD-62086.

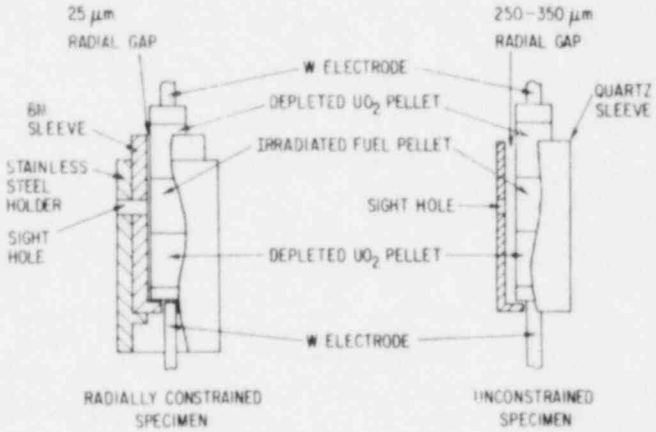

Fig. 7. Holders for Constrained (Left) and Unconstrained (Right) Specimens. Neg. No. MSD-223537.

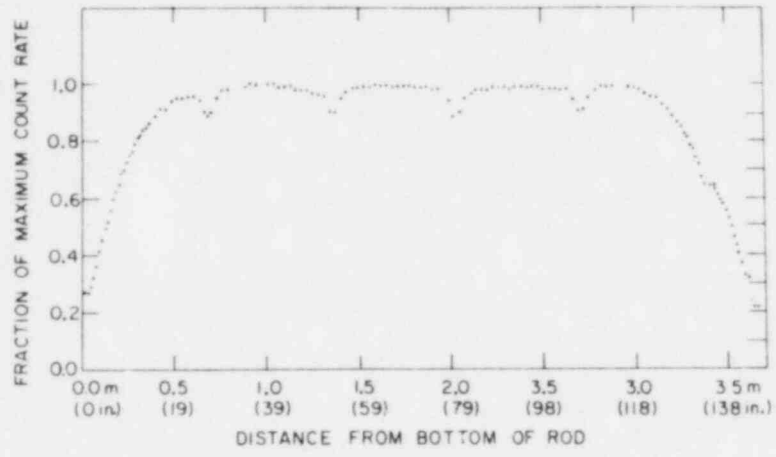

Fig. 8. Axial Gamma Scan of Robinson Fuel Rod F-7. Neg. No. MSD-62082.

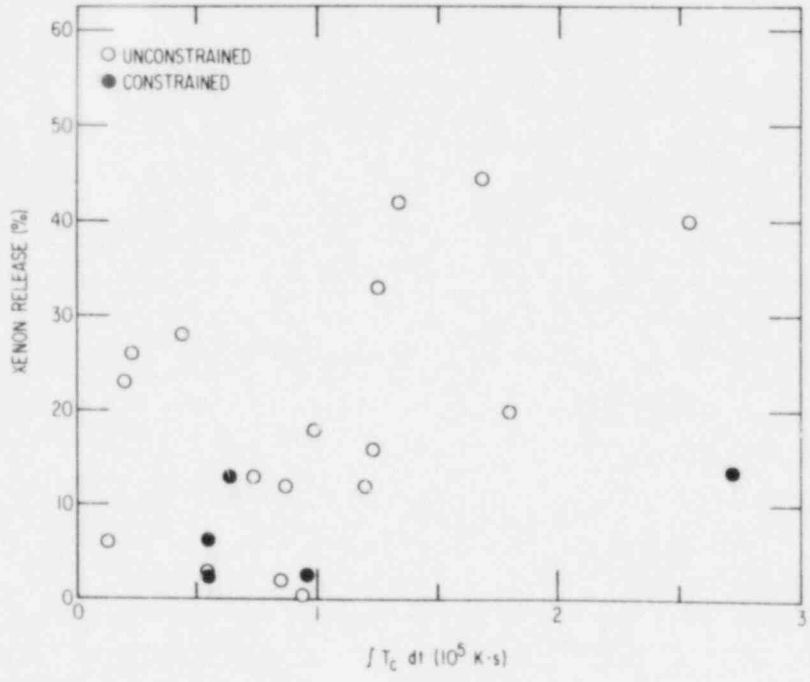

Fig. 9. Xenon Release as a Function of the Time Integral of Fuel Centerline Temperature for Unconstrained PCM Tests. Neg. No. MSD-223535.

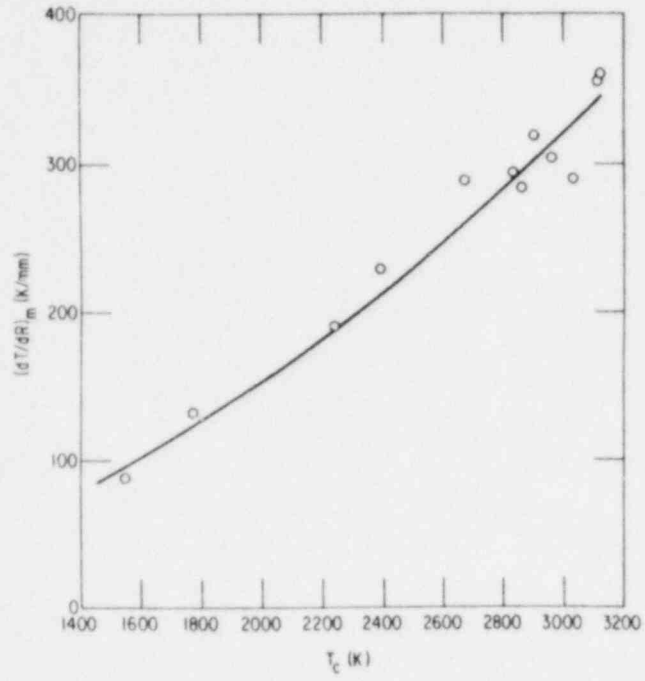

Fig. 10. Radial Temperature Gradient as a Function of Centerline Temperature for DEH Simulations of PCM Tests. Neg. No. MSD-223526.

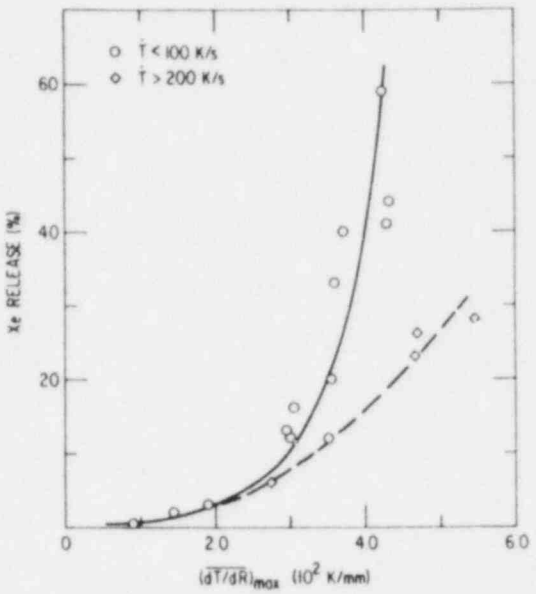

Fig. 11. Xenon Release as a Function of Radial Temperature Gradient for Unconstrained PCM Tests. Neg. No. MSD-198869.

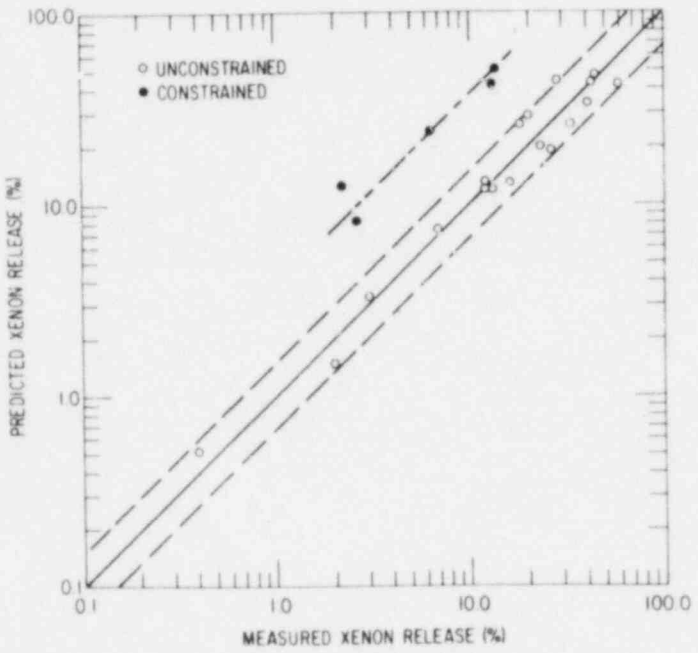

Fig. 12. Gas-release Predictions of the Empirical Correlation as a Function of Measured Values for PCM Tests. Neg. No. MSD-223530.

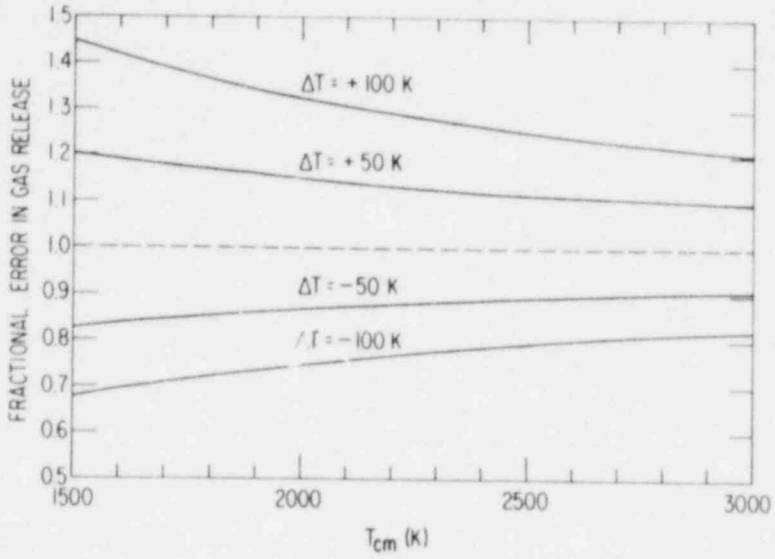

Fig. 13. Relative Error in Prediction of Gas-release Correlation for Assumed Errors in Calculated Temperature. Neg. No. MSD-223966.

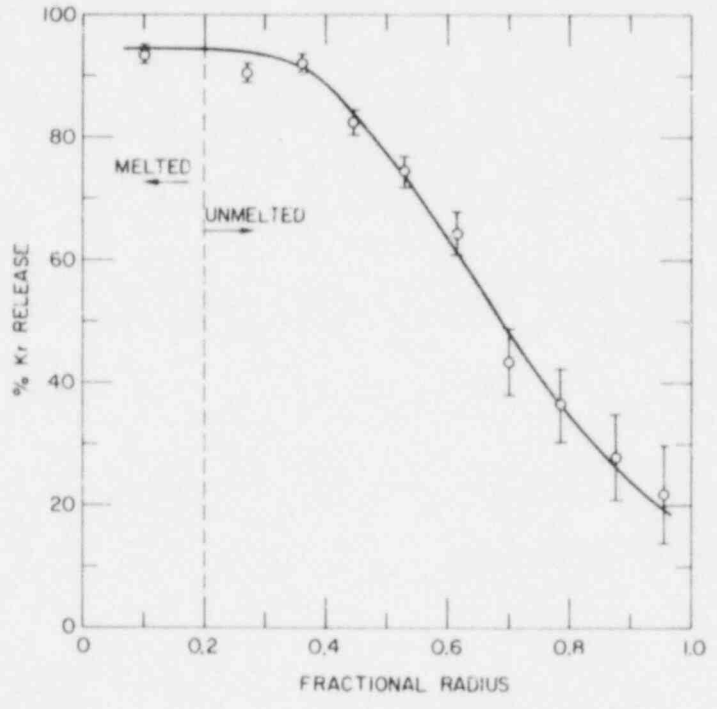

Fig. 14. Radial Profile of Transient Fission-gas Release for the Test-33 Fuel Specimen. ANL Neg. No. 306-78-236.

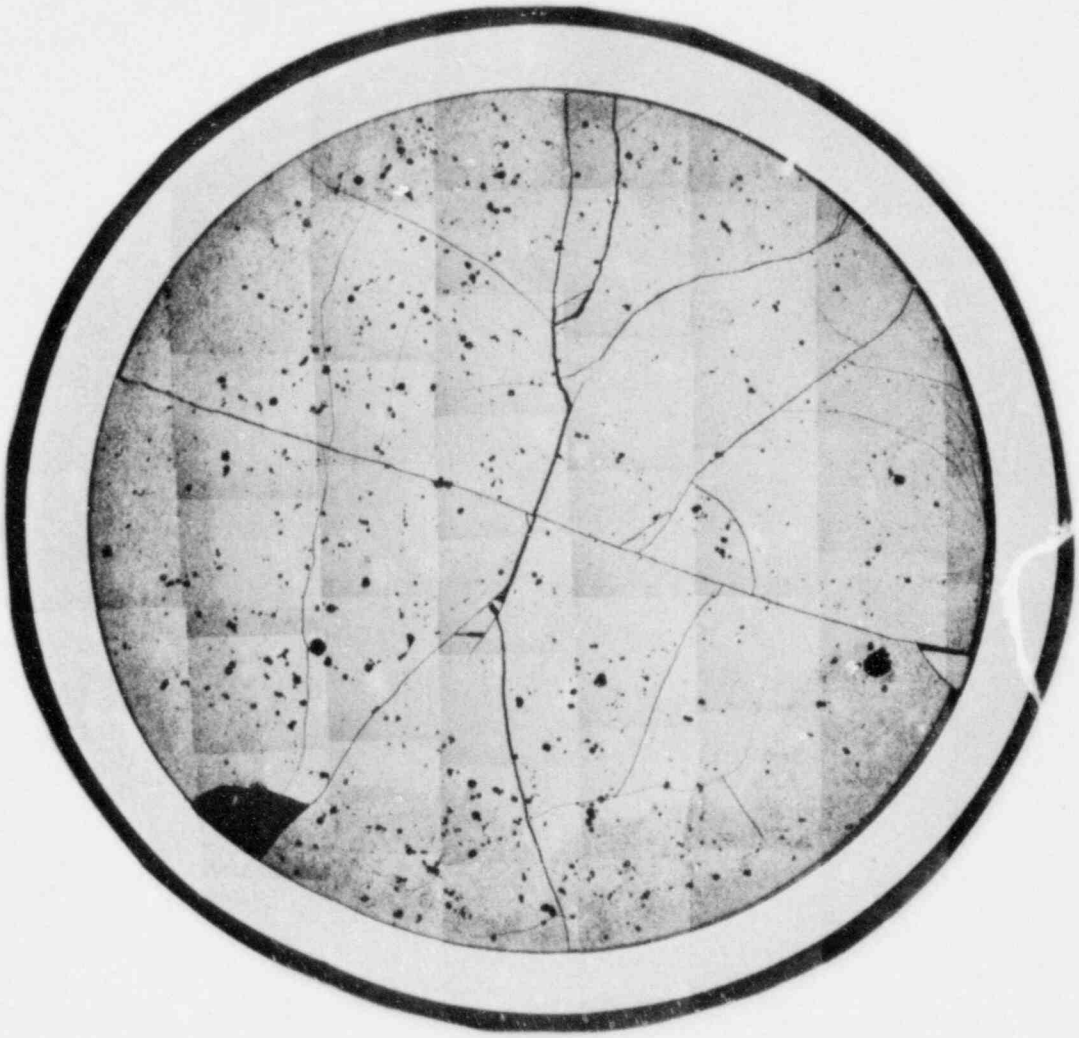

Fig. 15. Polished Transverse Section through the As-irradiated H. B. Robinson Fuel. Neg. No. MSD-185339.

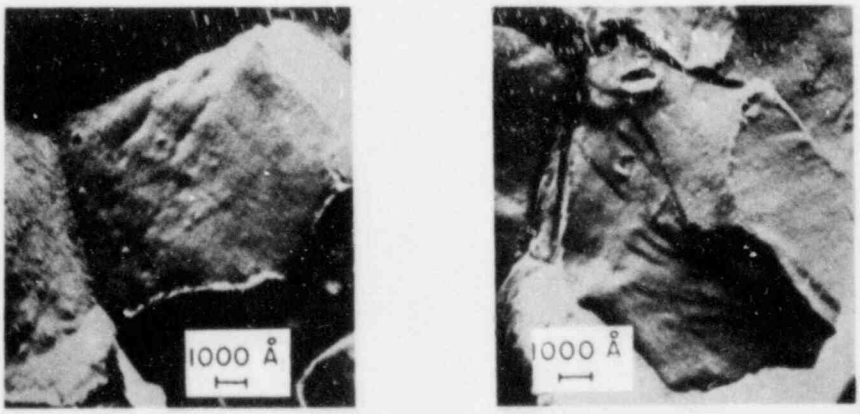

Fig. 16. Replica Electron Micrographs of Fission-gas Bubbles on the Grain Boundaries of the As-irradiated Robinson Fuel. Neg. No. MSD-185901.

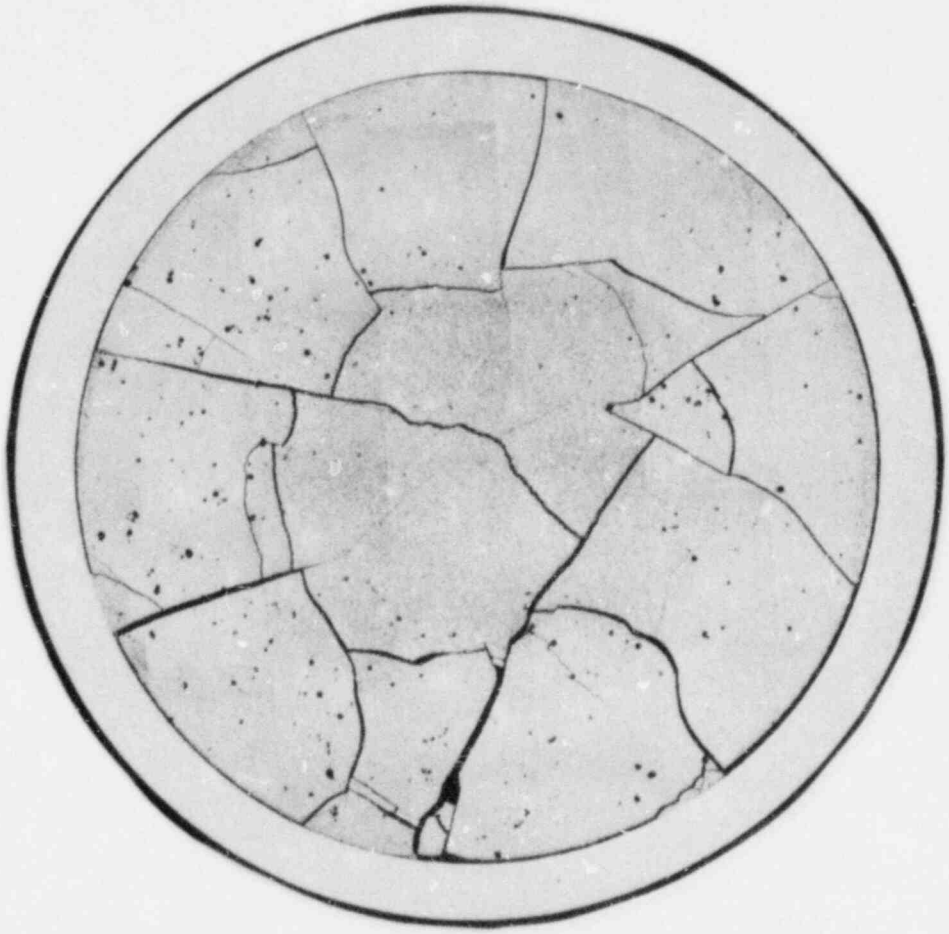

Fig. 17. Polished Transverse Section through the As-irradiated Saxton Fuel. Neg. No. MSD-192038.

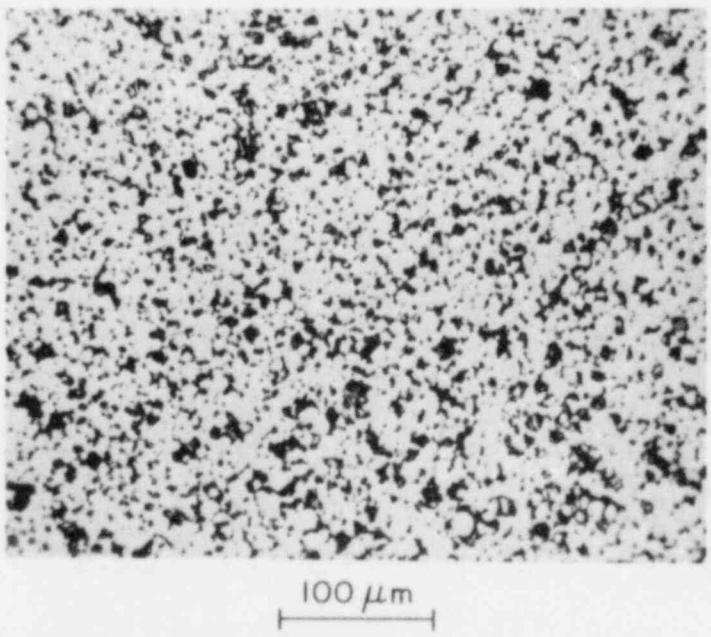

Fig. 18. Grain Structure and Intergranular Porosity in the Central Region of the Saxton Fuel. Neg. No. MSD-189804.

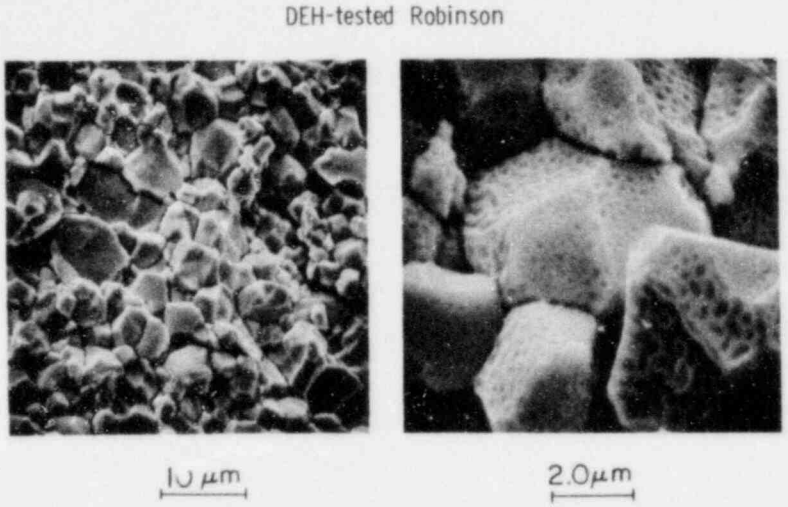

Fig. 19. Scanning-electron Fractographs of a Region of the Test-24 Fuel Heated to a Maximum Temperature of ∿1680 K. Neg. No. MSD-221168.

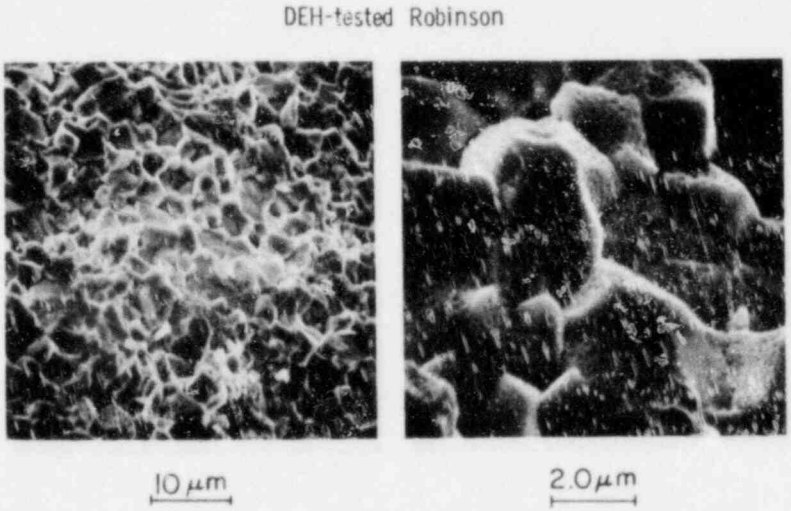

Fig. 20. Scanning-electron Fractographs of a Region of the Test-24 Fuel Heated to a Maximum Temperature of ∿1770 K. Neg. No. MSD-221170.

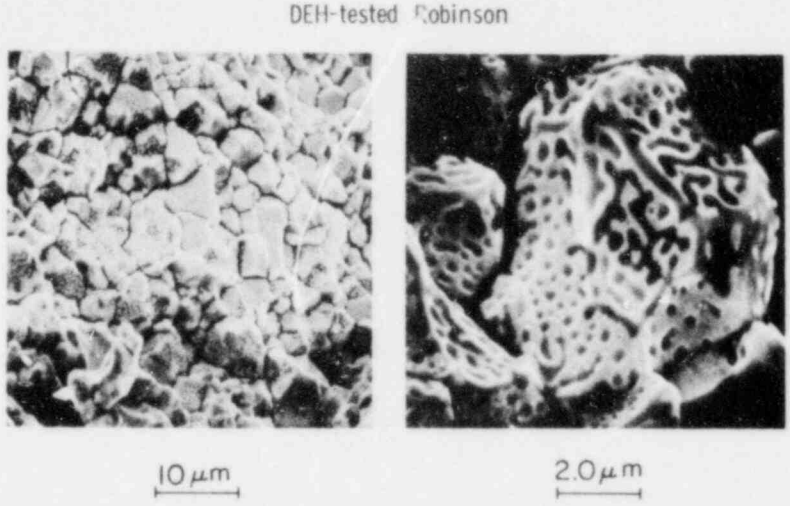

Fig. 21. Scanning-electron Fractographs of a Region of the Test-24 Fuel Heated to a Maximum Temperature of ∿1870 K. Neg. No. MSD-221169.

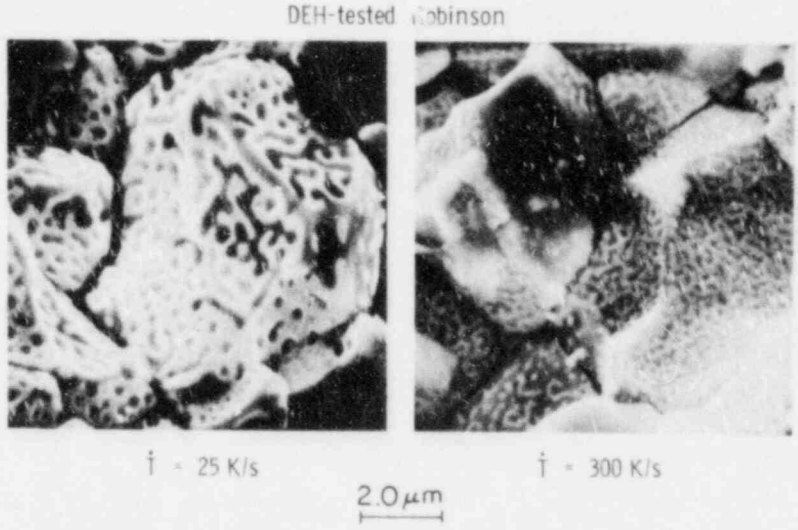

Fig. 22. Scanning-electron Fractographs Showing the Effect of Heating Rate on the Morphology of Grain-surface Channels. Neg. No. MSD-196174.

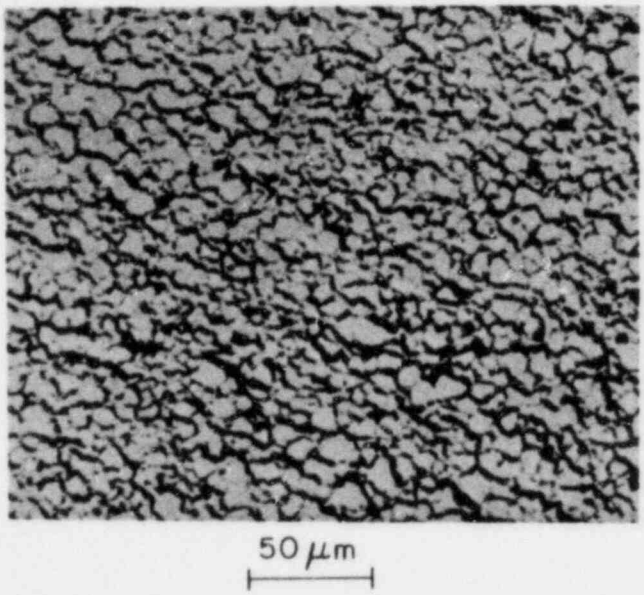

Fig. 23. Optical Micrograph of Microcracking in DEH-tested Fuel. Neg. No. MSD-197283.

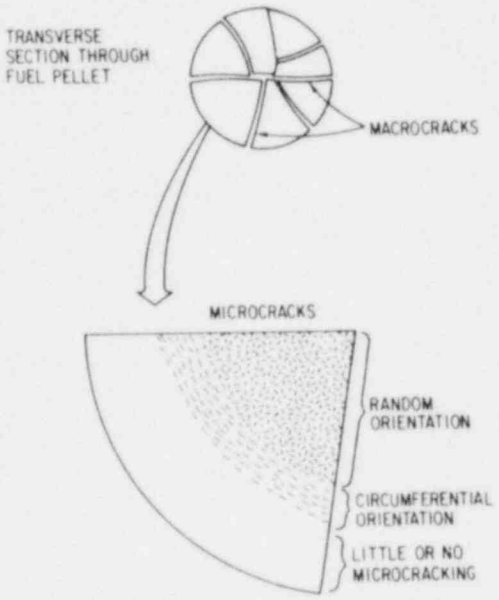

Fig. 24. Typical Pattern of Microcracking in Transient-tested Fuel. Neg. No. MSD-223525.

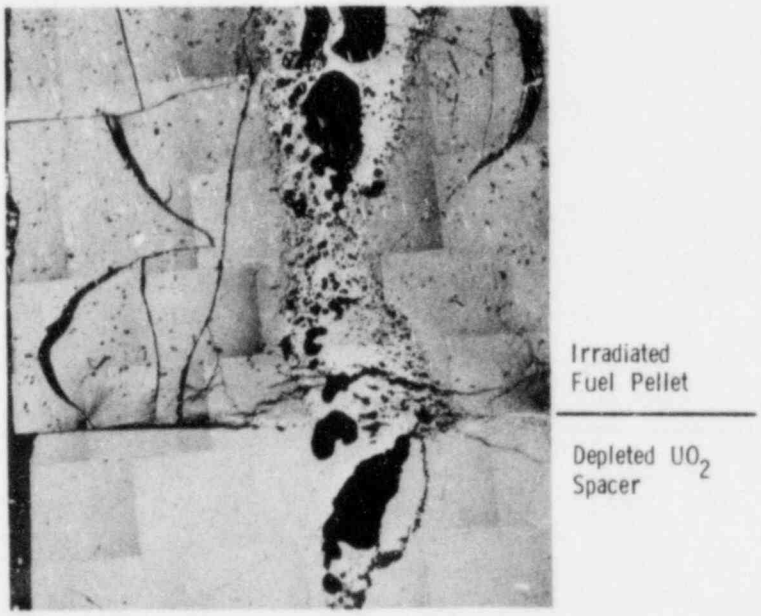

Fig. 25. Longitudinal Section through the Test 21 Specimen Showing Microcracking in the High-burnup Fuel (Top) and the Absence of Microcracking in the Depleted-UO_2 Spacer Pellet. Neg. No. MSD-188347.

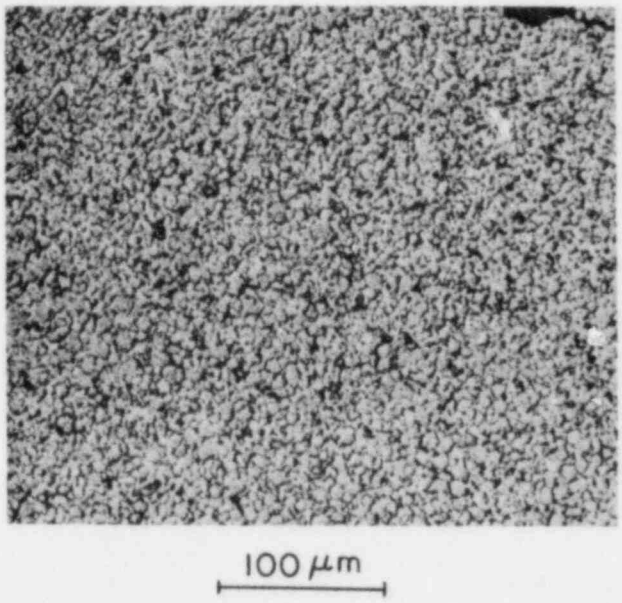

Fig. 26. Isotropic Intergranular Swelling in the Test-41 Fuel. Neg. No. MSD-195322.

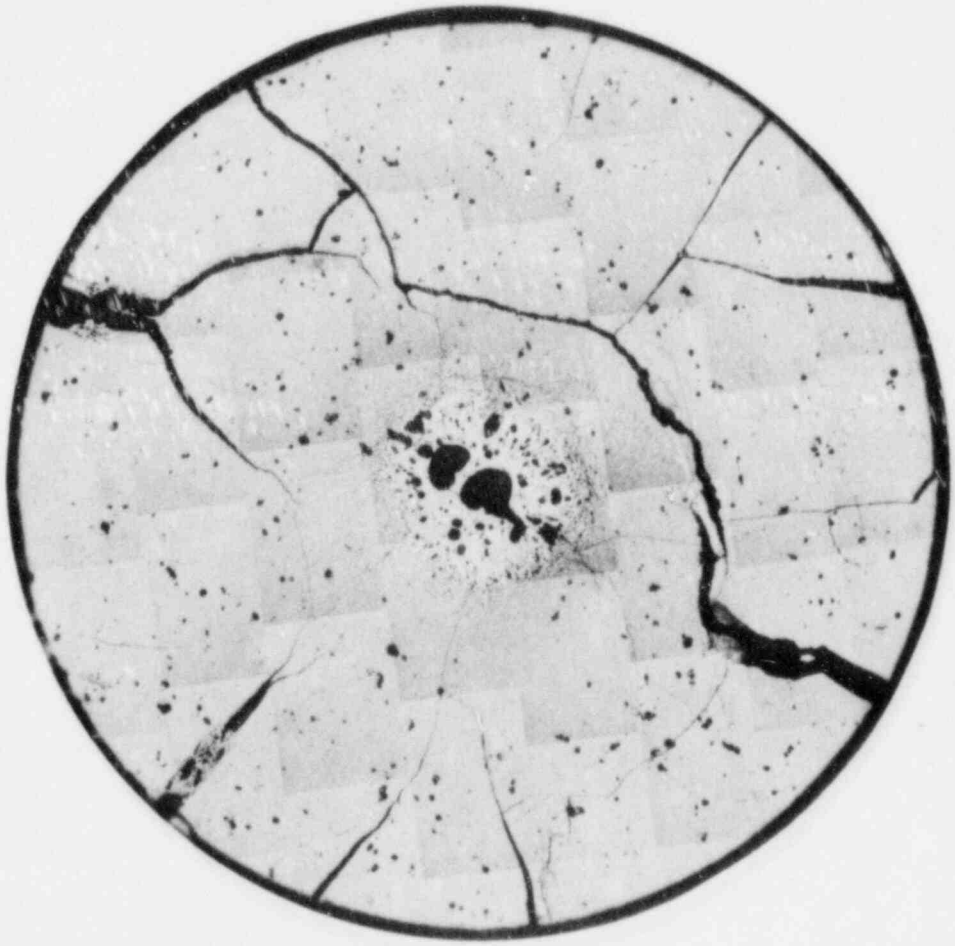

Fig. 27. Polished Transverse Section through the Test-33 (Robinson) Fuel. Neg. No. MSD-192035.

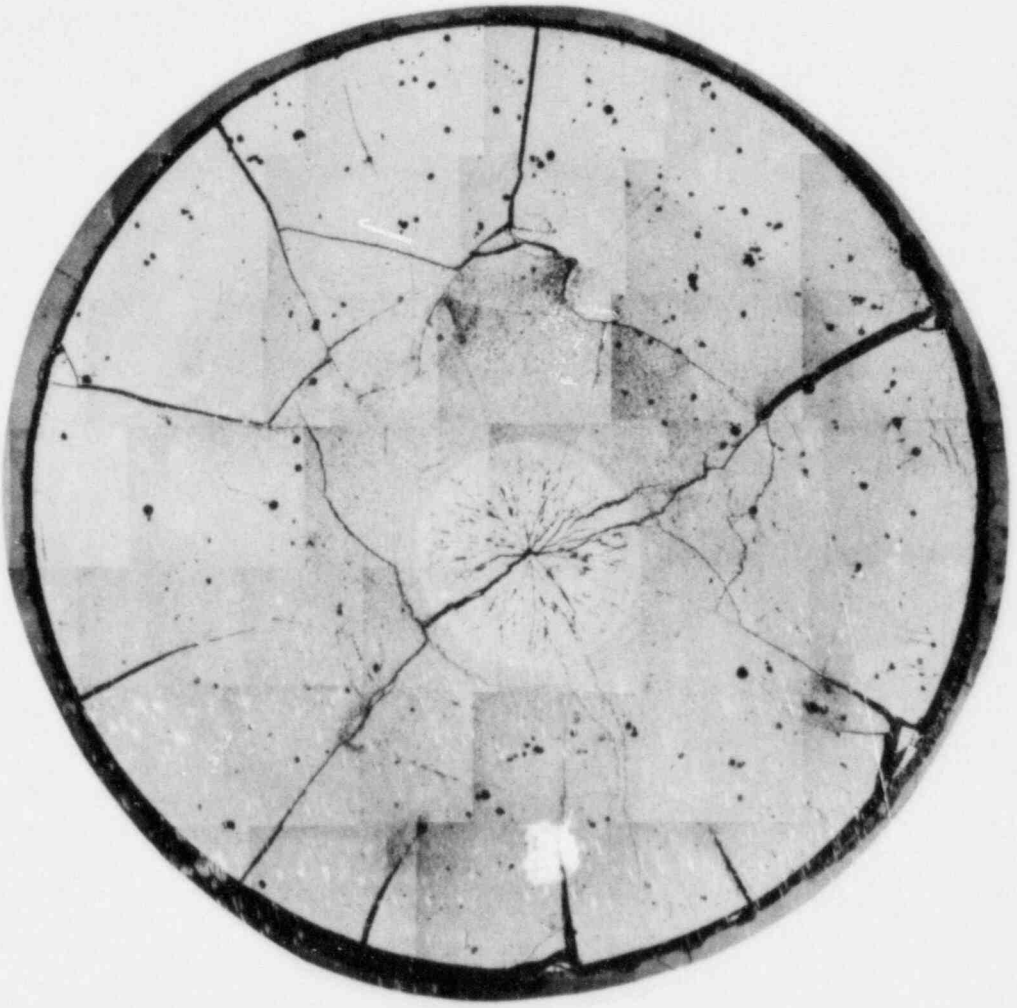

Fig. 28. Polished Transverse Section through the Test-35 (Saxton) Fuel. Neg. No. MSD-192085.

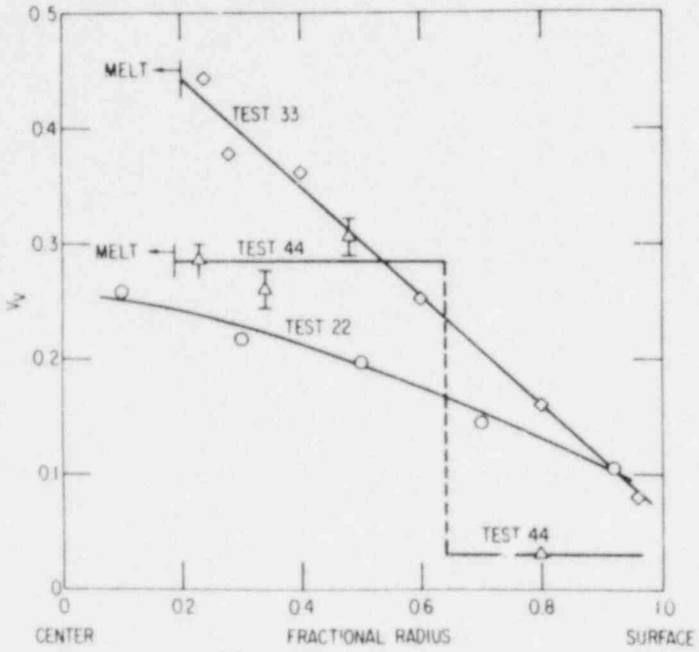

Fig. 29. Pore Volume Fraction (V_V) as a Function of Pellet Radius for Tests 22, 33, and 44. Neg. No. MSD-223533.

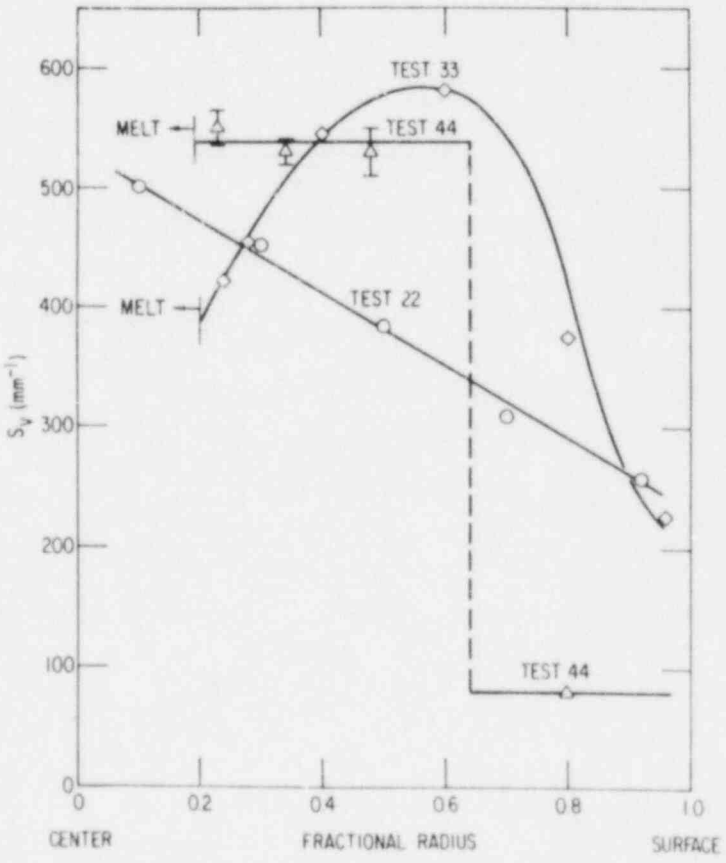

Fig. 30. Surface Area per Unit Volume of Intergranular Separations as a Function of Pellet Radius for Tests 22, 33, and 44. Neg. No. MSD-223534.

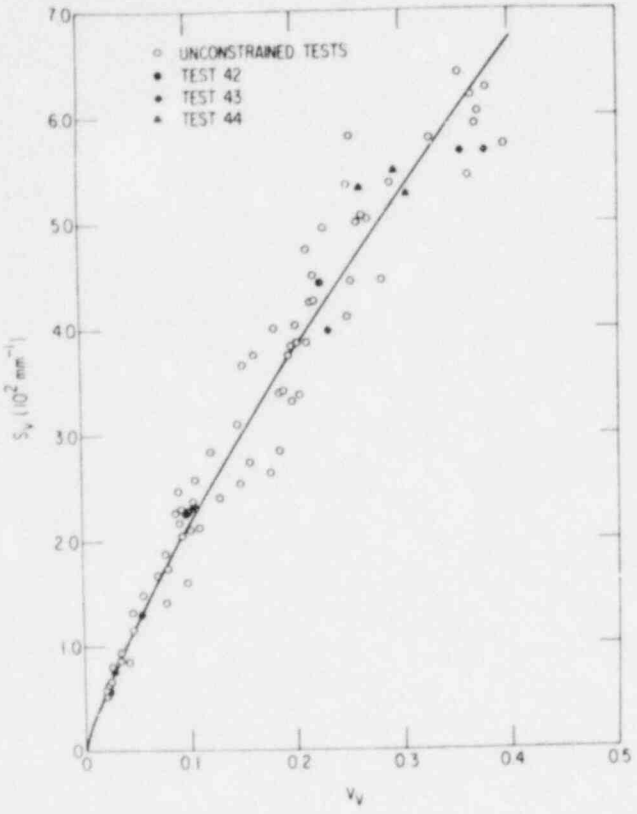

Fig. 31. Surface Area per Unit Volume of Intergranular Separations as a Function of Pore Volume Fraction for All Radial Zones in All PCM Tests. Neg. No. MSD-198864.

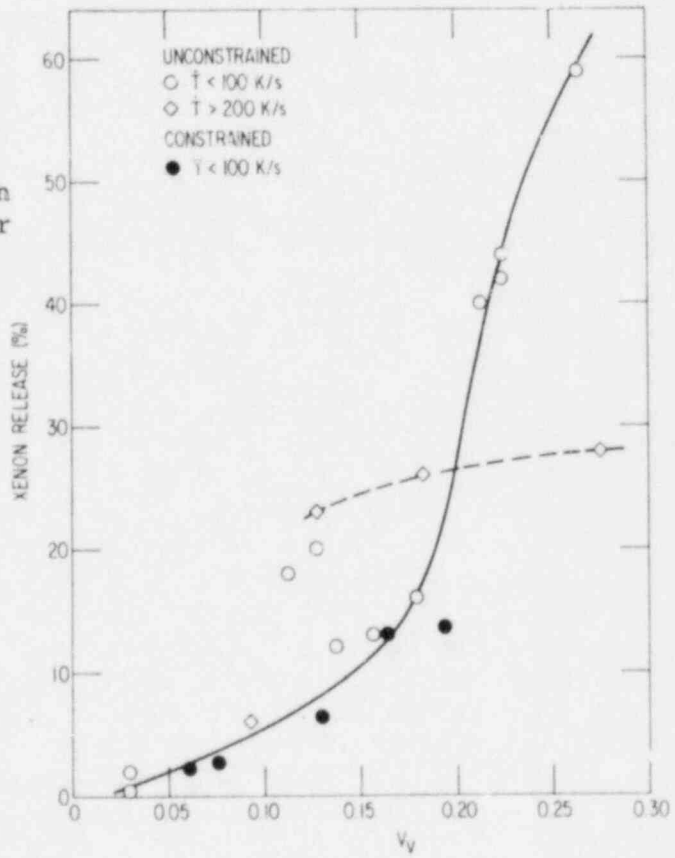

Fig. 32. Xenon Release as a Function of Pore Volume Fraction for DEH Tests. Neg. No. MSD-223532.

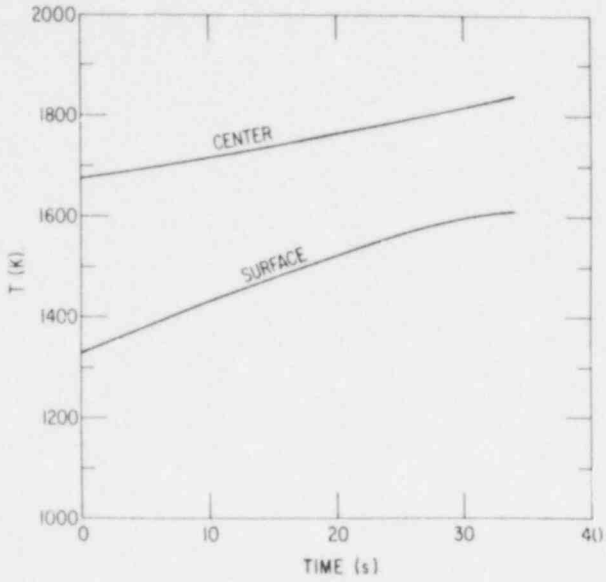

Fig. 33. Fuel Temperature History for LOCA Simulation (Test 48). Neg. No. MSD-223527.

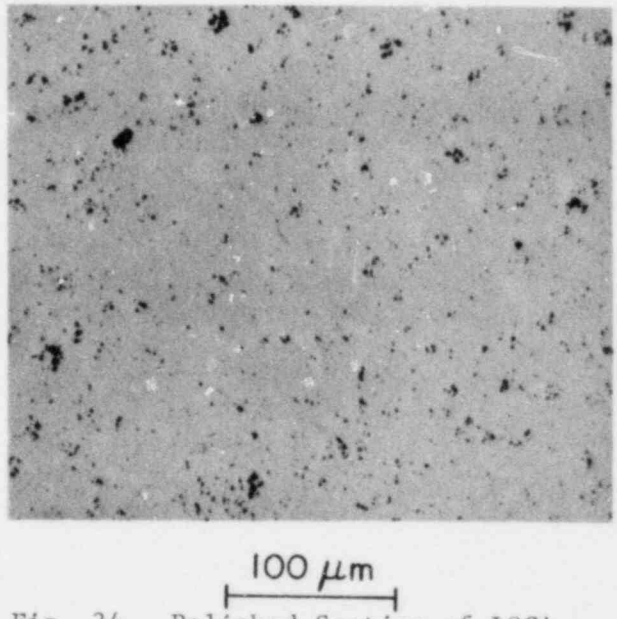

Fig. 34. Polished Section of LOCA-tested Fuel Showing Isolated Grain-boundary Bubbles. Neg. No. MSD-220569.

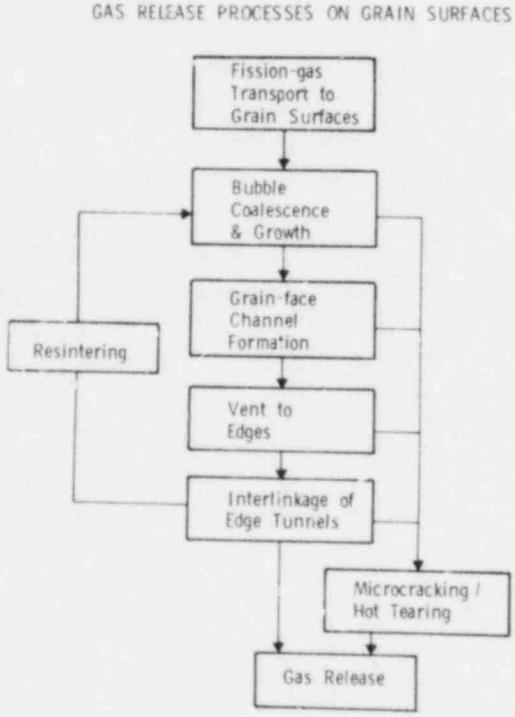

Fig. 35. Interrelationships among the Mechanisms Responsible for the Release of Grain-boundary Gas. Neg. No. MSD-221185.

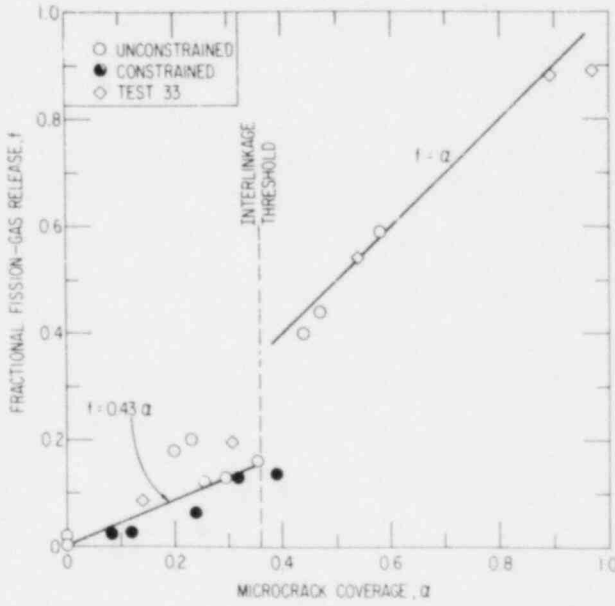

Fig. 36. Xenon Release as a Function of the Fraction of the Grain-boundary Area Occupied by Microcracks. Neg. No. MSD-223531.

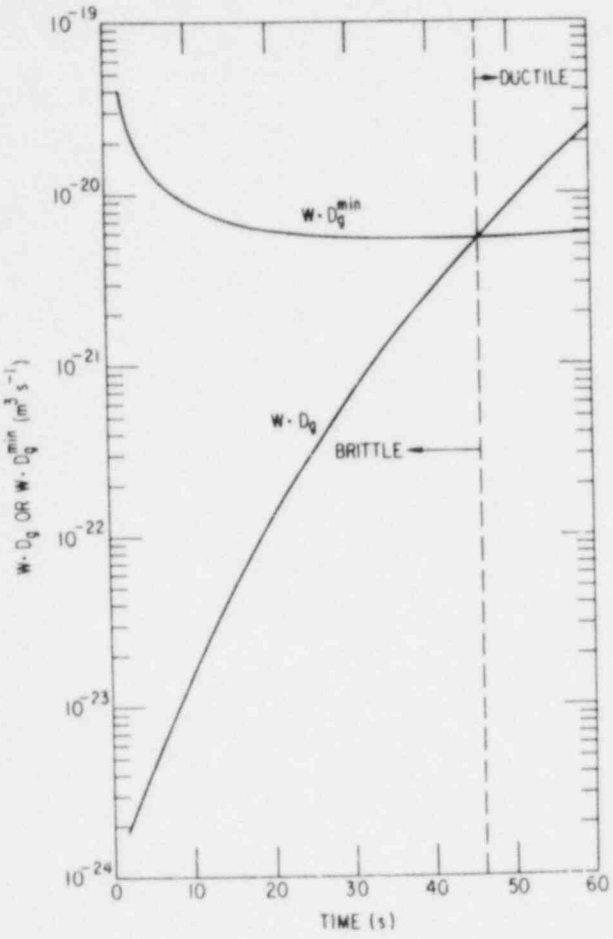

Fig. 37. Behavior of $w \cdot D_g$ and $w \cdot D_g^{min}$ During Test 32 at the Pellet Centerline. Neg. No. MSD-223523.

Fig. 38. Behavior of $w \cdot D_g$ and $w \cdot D_g^{min}$ During Test 32 at a Fractional Pellet Radius of 0.44. Neg. No. MSD-223524.

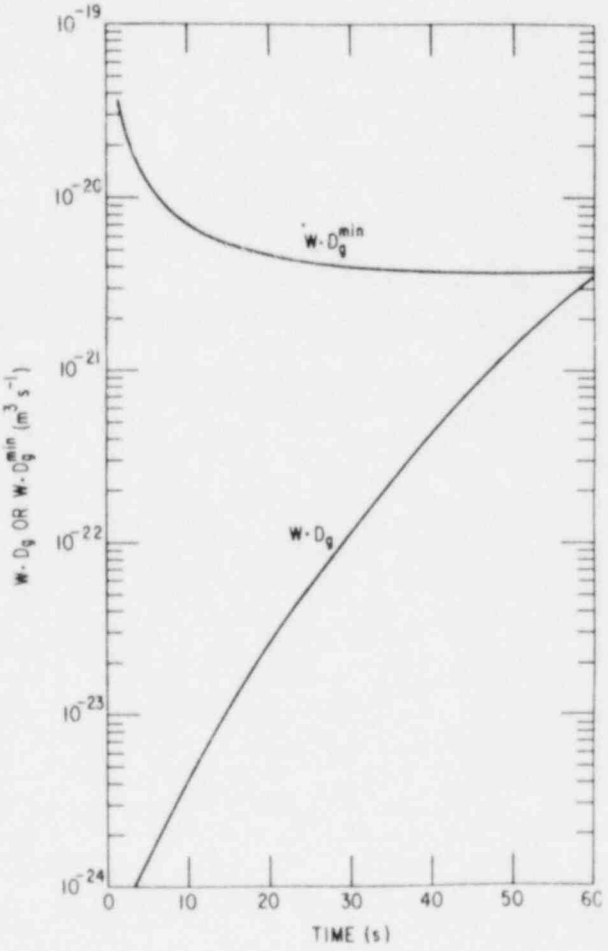

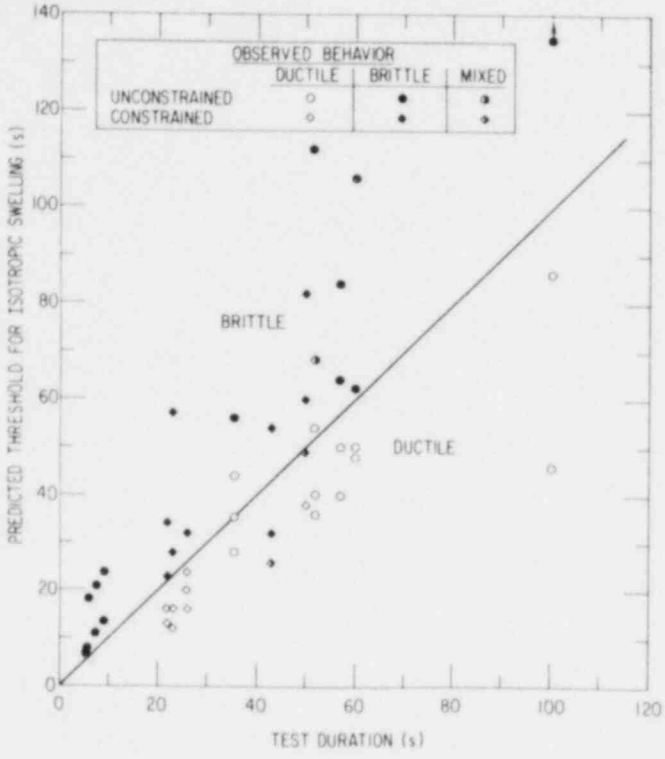

Fig. 39. Comparison of the Ductile/Brittle Model Predictions with Observed Behavior. Neg. No. MSD-223529.

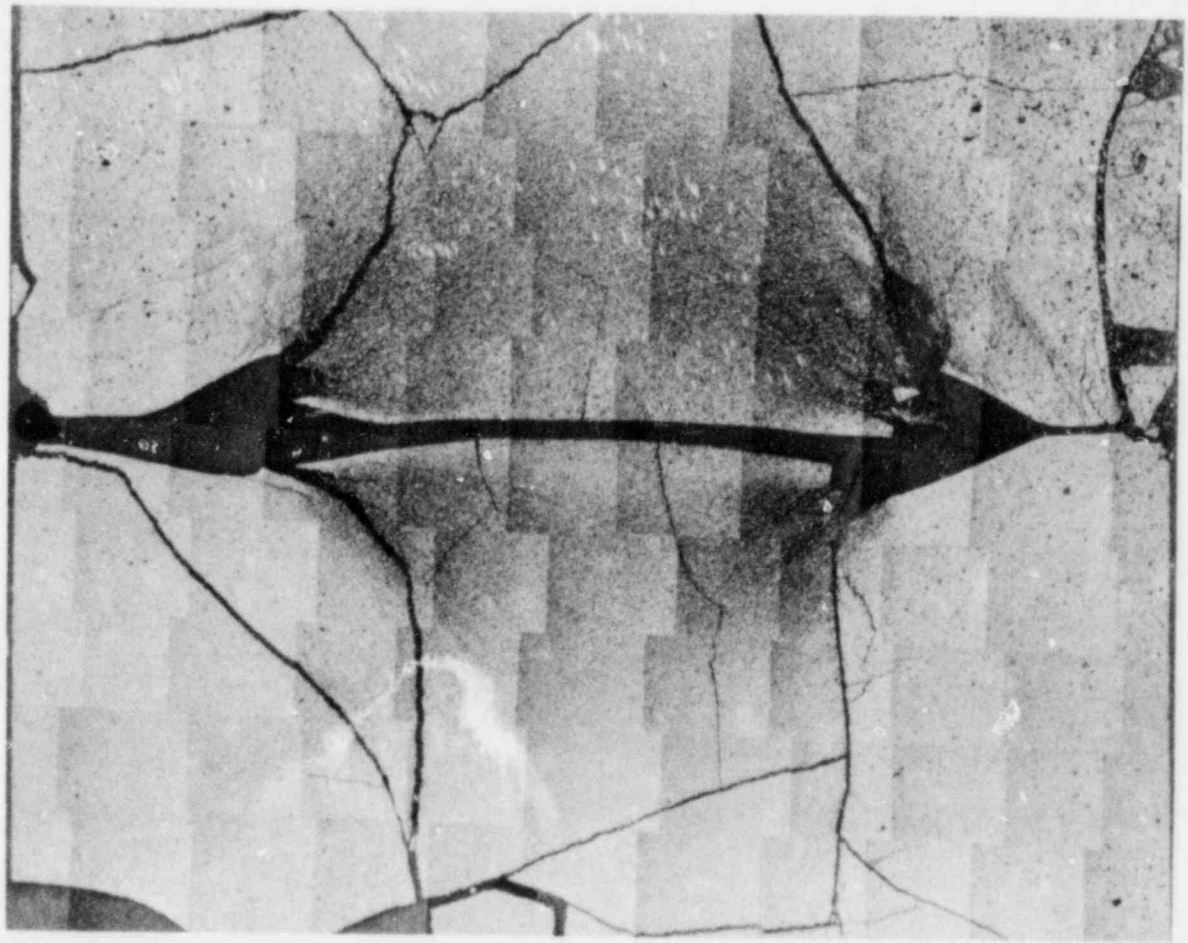

Fig. 40. Longitudinal Section through a Pellet-Pellet Interface of Dresden-3 Fuel after an In-reactor Power Transient. Neg. No. MSD-192541.

MICROCRACKING PRODUCED BY DEH
AND IN-REACTOR TRANSIENTS

DEH-TESTED ROBINSON

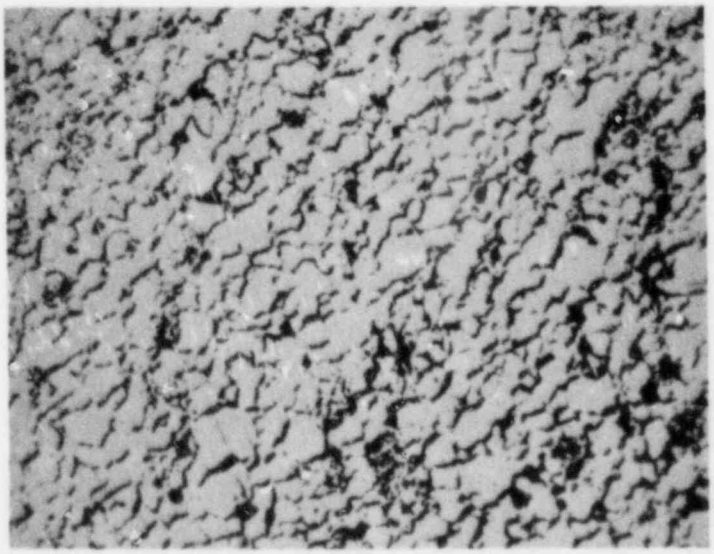

DRESDEN-3 100 μm

Fig. 41. Comparison of Microcrack Morphology in the Dresden-3 and DEH-tested Robinson Fuels. Neg. No. MSD-221167.

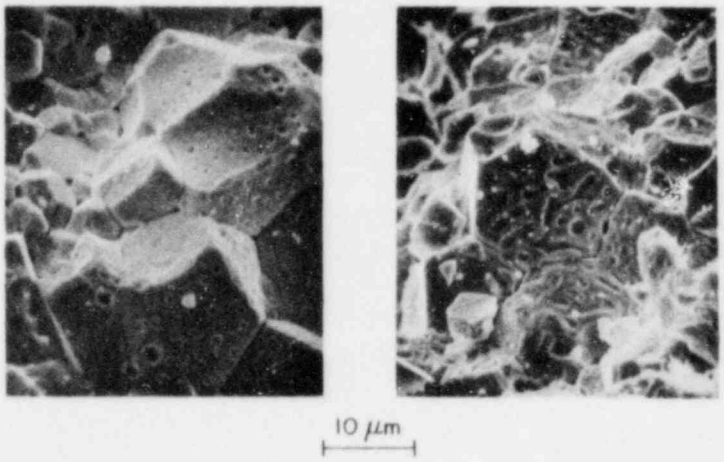

Fig. 42. Fractographs of Dresden-3 Fuel Showing Grain-surface Bubbles (left) and Channels (right).

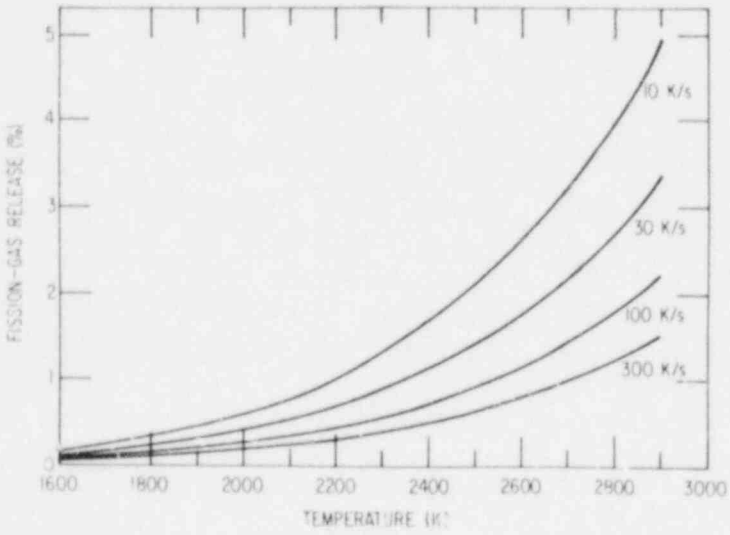

Fig. 43. Gas Release as a Function of Maximum Temperature for Conditions Typical of Anticipated Transients. Neg. No. MSD-223536.

Fig. 44. Effective Thermal Conductivity as a Function of Volume Fraction for Ellipsoids and Microcracks. Neg. No. MSD-22175.

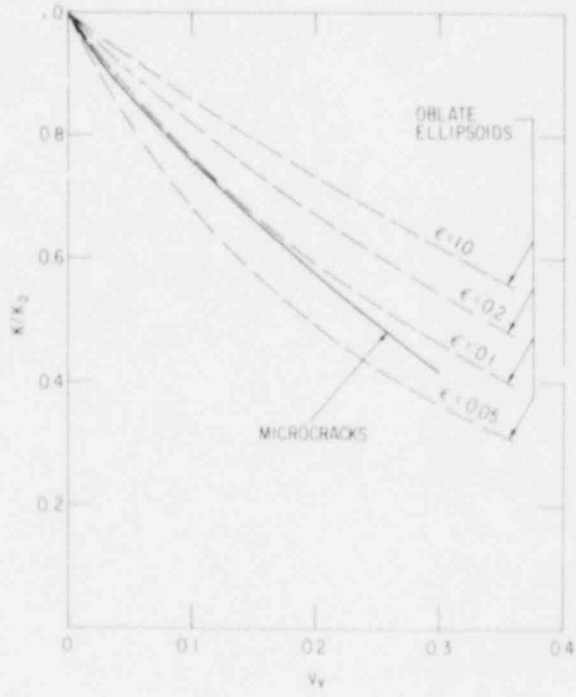

REFERENCES

1. "The Role of Fission Gas Release in Reactor Licensing," Core Performance Branch, U. S. Nuclear Regulatory Commission, Report NUREG-75/077 (Nov. 1975).

2. NRC/TMI Special Inquiry Group, "Three Mile Island: A Report to the Commissioners and to the Public," Vol. II, pp. 524-527.

3. Regulatory Guide 1.3, U. S. Nuclear Regulatory Comission, Office of Standards Development.

4. Regulatory Guide 1.4, U. S. Nuclear Regulatory Commission, Office of Standards Development.

5. Regulatory Guide 1.77, U. S Nuclear Regulatory Commission, Office of Standards Development.

6. S. M. Gehl, M. G. Seitz, and J. Rest, "Fission-gas Release from Irradiated PWR Fuel during Simulated PCM-type Accidents: Progress Report," U. S. Nuclear Regulatory Commission Report NUREG/CR-0088 and Argonne National Laboratory Report ANL-77-80 (May 1978).

7. S. M. Gehl, M. G. Seitz, L. R. Kelman, and J. Rest, "Relationship Between Fission-gas Release and Microstructural Change during Transient Heating of Pressurized Water Reactor Fuel," Proc. ANS Topical Mtg. on Thermal Reactor Safety, CONF-770708, Vol. 3, pp. 3-261 to 3-282 (1977).

8. O. D. Slagle, C. A. Hinman, and E. T. Weber, "Experiments on Melting and Gas Release Behavior of Irradiated Fuel," Hanford Engineering Development Laboratory Report HEDL-TME 74-17 (Sept. 1974).

9. C. A. Hinman and O. D. Slagle, "Ex-reactor Transient Fission Gas Release Studies," Fuel Pin PNL-2-4, Hanford Engineering Development Laboratory Report HEDL-TME-77-83 (May 1978).

10. G. Bandyopadhyay and J. A. Buzzell, "Microstructural Investigation of Mixed-oxide Fuels Subjected to Simulated Thermal-transient Conditions," Ceramic Microstructures, 1976, R. M. Fulrath and J. A. Pask, Eds., Westview Press, Boulder, CO, pp. 835-848 (1977).

11. R. G. Bellamy and J. E. Rich, "Grain-boundary Gas Release and Swelling in High Burnup Uranium Dioxide," J. Nucl. Mater. 33, 64-76 (1969).

12. H. Zimmerman, "Fission-gas Behavior in Oxide fuel Elements of Test Breeder Reactors," Nucl. Technol. 28, 127-133 (1976).

13. D. Stahl and T. J. Patrician, "Fission-gas Behavior during a Mild Overpower Transient," Argonne National Laboratory Report ANL-8069 (Feb. 1974).

14. J. Rest, "GRASS-SST: A Comprehensive, Mechanistic Model for the Prediction of Fission-gas Behavior in UO_2-base Fuels during Steady-state and Transient Conditions," U. S. Nuclear Regulatory Commission Report NUREG/CR-0202 and Argonne National Laboratory Report ANL-78-53 (June 1978).

15. J. Rest and S. M. Gehl, "The Mechanistic Prediction of Transient Fission-Gas Release from LWR Fuel," Nucl. Eng. Des. 56(1), 233-256 (1980).

16. K. Freund and W. Schikarski, "Der Direkt Elektrisch Geheizte UO_2 Brennstab," Kernforschungszentrum, Karlsruhe KfK-1031, EURFNR-773 (1970).

17. B. J. Wrona and E. Johanson, "Development of Direct Electrical Heating Apparatus to Study the Response of Nuclear Fuel to Applied Transients," Nucl. Technol. 29, 433 (1976).

18. D. G. Graczyk, G. Bandyopadhyay, S. M. Gehl, J. P. Hughes, and H. T. Goodspeed, "A Laser Microsampling Method for Determination of Retained Fission Gas in Irradiated Nuclear Fuels," Argonne National Laboratory Report ANL-79-86 (Oct. 1979).

19. J. A. Turnbull and M. O. Tucker, "Swelling in UO_2 Under Conditions of Gas Release," Phil. Mag. 30, 47 (1972).

20. M. O. Tucker, "A Simple Description of Interconnected Grain Edge Porosity," J. Nucl. Mater. 79, 199-205 (1979).

21. M. O. Tucker and R. J. White, "The Geometry of Interlinked Grain Edge Porosity," Res. Mechanica 1, 21-30 (1980).

22. M. O. Tucker, "The Transfer of Fission Gas Between Grain Faces and Edges in UO_2," J. Nucl. Mater. 75, 282-287 (1978).

23. M. O. Tucker, "Relative Growth Rates of Fission-gas bubbles on Grain Faces," J. Nucl. Mater. 78, 17-23 (1978).

24. J. C. Killeen, "Fission Gas Release and Swelling in UO_2 Doped with Cr_2O_3," J. Nucl. Mater. 88, 177-184 (1980).

25. S. M. Gehl, "Comparison of Fission Gas Release and Mechanical Behavior During Transient Nuclear and Electrical Heating of Light Water Reactor Fuel," U. S. Nuclear Regulatory Commission Report NUREG/CR-1001 and Argonne National Laboratory Report ANL-78-60 (June 1979).

26. J. T. Dusek, Argonne National Laboratory, personal communication.

27. S. Das, Argonne National Laboratory, unpublished information.

28. A. C. Hindmarsh, "GEAR--Ordinary Differential Equation System Solver," Lawrence Livermore Laboratory Report UCID-30001, Rev. 3 (Dec. 1974).

29. R. A. Lorenz, J. L. Collins, and S. R. Manning, "Quarterly Progress Report on Fission Product Release from LWR Fuel for the Period Oct.-Dec. 1975," Oak Ridge National Laboratory Report ORNL/TM-5290 (March 1976).

30. G. W. Gibson et al., "Characterization of UO_2-Zircaloy Fuel Rod Materials from the Saxton Reactor for Use in Power Burst Facility," Aerojet Nuclear Company Report ANCR-NUREG-1321 (Sept. 1976).

31. R. F. Canon, J. T. A. Roberts, and R. J. Beals, "Deformation of UO_2 at High Temperatures," J. Am. Ceram. Soc. 54, 105-112 (1971).

32. K. Maschke, H. Overhof, and P. Thomas, "A Note on Percolation Probabilities," Phys. Status Solidi 60 (6), 563-566 (1973).

33. R. J. DiMelfi and L. W. Deitrich, "The Effects of Grain Boundary Fission Gas on Transient Fuel Behavior," Nucl. Technol. 43, 328-337 (1979).

34. P. E. MacDonald et al., "Response of Unirradiated and Irradiated PWR Fuel Rods under Power-Cooling-Mismatch Conditions," EG&G Idaho, Inc. Report TREE-NUREG-1196 (Jan. 1978).

35. A. W. Cronenberg and T. R. Yackle, "An Assessment of Intergranular Fracture with Unrestructured UO_2 Fuel due to Film Boiling Operation," EG&G Idaho, Inc. Report NUREG/CR-0595, TREE-1330 (March 1979).

36. V. Pasupathi et al., "Determination and Microscopic Study of Incipient Defects in Irradiated Power Reactor Fuel Rods," Electric Power Research Institute Report EPRI NP-812, Project 829, Final Report (July 1978).

37. W. N. Bishop et al., "Fission Product Release from the Fuel Following the TMI-2 Accident," presented at ANS/ENS Thermal Reactor Safety Meeting, Knoxville, TN, April 1980.

38. M. Ishikawa et al., "NSRR Experiments on LWR Fuel Behavior under Reactivity-Initiated Accident Condition," Proc. ANS Topical Meeting on Thermal Reactor Safety, Sun Valley, ID, July 31-August 4, 1977, Vol. 3, pp. 29-42.

39. P. E. MacDonald et al., "Light Water Reactor Fuel Response During Reactivity-Initiated Accident Experiments," Proc. ANS Topical Meeting on Light Water Reactor Fuel Performance, Portland, OR, April 29-May 3, 1979, pp. 218-226.

40. American National Standard N18.2 - 1973.

41. P. Knudsen, C. Bagger, and H. Carlson, "PWR-Type Overpower Tests at 1620 GJ/kgU (18,800 MWD/MTU)," Proc. ANS Topical Meeting on Light Water Reactor Fuel Performance, Portland, OR, April 29-May 3, 1979, pp. 264-274.

42. M. Mogard et al., "The Studsvik Inter-Ramp Project, an International Power Ramp Experimental Study," ibid., pp. 284-294.

43. W. J. Leech and R. S. Kaiser, "The Effects of Fission Gas Release on PWR Fuel Rod Performance," presented at the IAEA Specialists' Meeting on Water Reactor Fuel Element Performance Computer Modeling, Blackpool, UK, March 16-21, 1980.

44. S. Pati and S. E. Ritterbusch, "Fission Gas Release During Anticipated Transients," ibid.

45. A. B. G. Washington, "Preferred Values for the Thermal Conductivity of Sintered Ceramic Fuels for Fast Reactor Use," UKAEA TRG-Report 2236 (Sept. 1973).

46. G. P. Marino, "The Porosity Correction Factor for the Thermal Conductivity of Ceramic Fuels," J. Nucl. Mater. 38, 178-190 (1971).

47. J. Maxwell, "A Treatise on Electricity and Magnetism," Vol. 1, Dover Publications, Inc., New York, p. 452 (1958).

48. H. Fricke, Phys. Rev. 24, 575-587 (1924).

APPENDIX A
THE EFFECT OF MICROCRACKING ON FUEL THERMAL CONDUCTIVITY

The extensive microcracking that occurs during transient heating has a substantial effect on fuel thermal conductivity. An estimate of the magnitude of this effect was needed for the transient temperature calculations in the DEHTTD code. In the course of the project, several methods for estimating thermal conductivity were investigated. The model described below was used for the temperature calculations presented elsewhere in this report. The model is both simple and realistic.

The model is based on the assumption that microcracks obstruct the radial flow of heat through the fuel by an amount proportional to the surface area of the microcracks. The assumption follows naturally from the observation that the microcracks can be approximated as disks with their flat surfaces approximately normal to the direction of heat flow. The thermal conductance of the microcracks is assumed to be negligible on the basis of (1) the low conductivity of the xenon fill gas and (2) the small ΔT, and the resulting small radiative heat transfer, across the 1-μm width of the cracks.

To apply the model, quantitative stereology measurements are used to determine the microcrack surface area as a function of radius at the end of the transient. During the transient, the microcracks are assumed to form and grow linearly with time, until the maximum extent of microcracking is achieved at the time corresponding to maximum power input. The extent of microcracking is assumed to be constant for the remainder of the transient.

The assumptions listed above lead to equations of the form

$$K_{eff}(T,R,t) = K_o(T)\left[1 - \beta \frac{t}{t_m} S_v(R)\right] \qquad (t < t_m) \qquad \text{(A1)}$$

and

$$K_{eff}(T,R,t) = K_o(T)[1 - \beta S_v(R)] \qquad (t > t_m), \qquad \text{(A2)}$$

where $K_{eff}(T,R,t)$ is the effective thermal conductivity used in DEHTTD; K_o is the temperature-dependent thermal conductivity obtained from Ref. 43; β is an empirically determined constant; t is the elapsed time during the transient; t_m is the time at which power input is a maximum; and $S_v(R)$ is the position-dependent microcrack surface area per unit volume, in units of mm^{-1}.

In practice, $S_v(R)$ is obtained by fitting a cubic polynomial to the measured S_v values. Measured values are usually available at four to six discrete radial positions. The cubic fit was used for $R_1 < R < R_N$, where R_1 denotes the innermost and R_N the outermost locations at which S_v measurements are available. For $R < R_1$, $S_v(R)$ is assumed equal to $S_v(R_1)$. Similarly, for $R > R_N$, $S_v(R)$ is taken to be equal to $S_v(R_N)$. These restraints prevent the inadvertent use of unrealistic values of $S_v(R)$.

The constant β was determined by matching the calculated and observed melt radii in test 33. The resulting value, i.e., $\beta = 1.1 \times 10^{-3}$, was used for all other DEH tests.

The only direct means of checking the model is by comparing the calculated and observed melt radii for tests in which central melting occurred. The agreement in such cases is within the resolution limit of the ten-node grid used in the DEHTTD code.

As a further check on the model, the thermal conductivity predictions were compared with an analysis by Marino[46] of the porosity correction for thermal conductivity. This approach is based on the Maxwell field equations.[47,48] The porosity correction factor for isolated, randomly oriented, oblate ellipsoids of varying aspect ratio ε is presented as a function of pore volume fraction in Fig. 44. Also shown is the correction factor obtained from Eq. (A2), using the substitution $V_v = 1.35 \times 10^{-4} S_v^{1.228}$ (see Section II.B.3 and Fig. 30). Note that the microcrack model closely approximates the curve for $\varepsilon = 0.1$ for $V_v < 0.2$. At larger volume fractions, the microcrack curve moves toward flatter aspect ratios. Microcracks observed in the DEH tests have aspect ratios in the range of 0.1, and resemble oblate ellipsoids in this respect, although the microcracks are interconnected. The decrease in ε at high V_v values is consistent with the latter stages of the microcracking process, in which crack propagation occurs with no accompanying change in crack width. Thus, a linear relationship between microcracking and thermal conductivity gives results that agree with a theoretical treatment of the porosity correction factor.

Locally, the volume fraction of microcracks can exceed 0.25. In this case, the thermal conductivity will be $\sim$50% of the value of dense fuel. A change of this magnitude will have a strong effect on calculated temperature profiles. As an example, DEHTTD calculations without the correction factor gave errors of >600 K in center temperature. The need for a correction factor is not limited to electrical heating. A correction to thermal conductivity is also required for nuclear transients in which microcracking impedes radial heat flux.

APPENDIX B

TABULATED DATA FOR DEH TESTS

Table BI
Summary of PCM Conditions and Results

Test	Duration, s	Average Centerline Heating Rate, K/s	Initial Centerline Temp., K	Max. Centerline Temp., K	Max. Radial Temp. Gradient, K/mm	$\int T_c dt$, K-s	Total Xe Release, %	Fractional Melt Radius	Xe Release from Unmelted Fuel, %	Pore Volume Fraction, V_v	Pore-Solid Surface Area, Sv^{-1} m
21	68	3.0	1500	-	432	1.68	50.0	0.33	44	0.244	406
22	36	18.6	1500	2170	163	0.742	13.1	-	13.1	0.155	332
23	28	26.4	1500	2240	191	0.542	3	-	3		
24	52	26.2	1610	2970	304	1.20	12	-	12	0.137	260
25	55	35	1500	-	430	1.34	48	0.33	42		
26	54	35	1500	-	426	1.31	61	0.32	59	0.264	431
27	54	30	1500	3120	360	1.25	33	-	33		
29	59	11	1130	1760	132	0.853	2.0	-	2.0	0.03	69
30	70	6	1130	1550	88	0.938	0.4	-	0.4	0.03	69
31	71	16	1960	3110	355	1.80	20.1	-	20.1	0.127	305
32	60	21	1580	2860	284	1.23	16.1	-	16.1	0.179	300
33	100	22	1650	-	370	2.54	40	0.20	40	0.213	421
35[a]	37	45	1500	-	300	0.870	16	0.20	12		
37	5.8	234	1670	3030	290	0.130	5.9	-	5.9	0.093	224
38	7.7	275	1590	-	419	0.199	34	0.38	23	0.127	264
39	15.3	225	1650	-	500	0.436	44	0.47	28	0.274	496
40	8.8	240	1650	-	404	0.232	37	0.38	26	0.182	334
41	35.5	84.2	1570	-	387	0.994	21.0	0.19	18	0.113	250
42	25.8	53.1	1530	2900	319	0.549	2.2	-	2.2	0.061	152
43	22.8	155	1570	-	472	0.643	17.2	0.22	13	0.164	289
44	22.2	101	1550	-	396	0.554	9.7	0.19	6.3	0.130	252
49	97.0	58.8	1120	-	439	2.72	19.1	0.25	13.5	0.194	313
51	50.3	16.1	1570	2380	229	0.962	2.6	-	2.6	0.077	149

[a]Saxton Fuel.

Table BII

Summary of LOCA Test Conditions and Results

	Test	
	48	53
Duration, s	34	40
Avg. Centerline Heating Rate, K/s	4.9	3.5
Avg. Surface Heating Rate, K/s	8.4	6.4
Init. Centerline Temp., K	1670	1710
Max. Centerline Temp., K	1850	1850
Init. Radial Temp. Gradient, K/mm	80.8	77.9
Final Radial Temp. Gradient, K/mm	63.1	58.9
Xe Release, %	1.2	0.2

Distribution for NUREG/CR-2777 (ANL-80-108)

Internal:

E. S. Beckjord
C. E. Till
B. R. T. Frost
R. W. Weeks
F. A. Nichols
J. Rest
L. A. Neimark
G. Fenske
L. W. Deitrich
C. E. Johnson
C. H. Bowers
R. J. DiMelfi
J. M. Kramer
S. M. Gehl (10)
Y. Y. Liu
H. C. Tsai
E. M. Stefanski
ANL Patent Dept.
ANL Contract File
ANL Libraries (3)
TIS Files (6)

External:

NRC Washington, for distribution per R3 (320)
DOE-TIC (2)
Manager, Chicago Operations Office, DOE
President, Argonne Universities Association
Materials Science Division Review Committee:
G. S. Ansell, Rensselaer Polytechnic Inst., Troy, N. Y. 12181
A. Arrott, Simon Fraser University, Burnaby, B. C., Canada V5A 1S6
R. W. Balluffi, Massachusetts Inst. of Technology, Cambridge, Mass. 02139
A. L. Bement, Jr., TRW, Inc., 23555 Euclid Ave., Cleveland, O. 44117
G. J. Fonken, University of Texas at Austin, Austin, Tex. 78712
C. Laird, University of Pennsylvania, Philadelphia, Pa. 19174
M. E. Shank, Pratt & Whitney, East Hartford, Conn. 06108
P. G. Shewmon, Ohio State University, Columbus, Ohio 43210
A. R. C. Westwood, Martin Marietta Labs., 1450 S. Rolling Rd., Baltimore, Md. 21227